DOT/FAA/TC-18/31

Federal Aviation Administration
William J. Hughes Technical Center
Aviation Research Division
Atlantic City International Airport
New Jersey 08405

High-Energy Wide-Area Blunt Impact Damage Formation to Stiffened-Skin Composite Structure

February 2019

Final Report

U.S. Department of Transportation
Federal Aviation Administration

NOTICE

Technical Report Documentation Page

1. Report No.	2. Government Accession No.	3. Recipient's Catalog No.
DOT/FAA/TC-18/31		

4. Title and Subtitle	5. Report Date
High-Energy Wide-Area Blunt Impact Damage Formation to Stiffened-Skin Composite Structure	February 2019
	6. Performing Organization Code

7. Author(s)	8. Performing Organization Report No.
Hyonny Kim, Zhi M. Chen, and Gabriela K. DeFrancisci	

9. Performing Organization Name and Address	10. Work Unit No. (TRAIS)
Department of Structural Engineering UC San Diego 9500 Gilman Drive #0085 La Jolla, CA 92093-005 USA	11. Contract or Grant No.

12. Sponsoring Agency Name and Address	13. Type of Report and Period Covered
FAA Seattle Headquarters 2200 S 216th St Des Moines, WA 98198	Final Report
	14. Sponsoring Agency Code AIR-600

15. Supplementary Notes

The FAA William J. Hughes Technical Center Aviation Research Division COR was Lynn Pham.

16. Abstract

Ongoing research at UC San Diego has focused on understanding the formation of damage to composite structures when subjected to blunt impact sources. Impact sources of interest are those acting over a wide area and potentially affecting multiple structural elements, but leaving little or no externally visible signs of the damage. Specifically, the severe impact of carbon/epoxy composite fuselage structures by ground service equipment (GSE) having soft/rubber-covered bumpers constitutes the high-energy wide-area blunt impact problem, which is the focus of the report. New-generation aircraft are constructed with high-strength composite skins, which have much lower tendency to form permanent dents, relative to aluminum alloy skins. Observations of Los Angeles International Airport ground operations were first conducted, which served to provide information on the types of scenarios and GSE posing a threat to aircraft. Composite test panel specimens were designed, following industry input, to include key internal structural features such as co-cured stringers, shear ties, and frames. The largest specimens were
1.8 x 2.4 m overall dimension, having four stringers and five frames. These, together with smaller-sized (1 x 1 m) stringer panel specimens were tested under both quasi-static and dynamic rate loading, up to 0.5 m/s (1.1 miles/hour). Resulting damage and visibility of this damage were dependent on the impactor stiffness (hard aluminum vs. rubber-covered), location of contact relative to stringers (directly on stringers vs. mid-skin bay between stringers), and as speed of loading. Hard-surface impactors are able to initiate and develop local surface cracking/penetration, whereas soft rubber-covered impactors allow for much higher loading without externally visible skin cracking, often resulting in significant internal damage modes, such as shear-tie delamination and crushing/bending failure, frame cracks, and stringer delamination. Furthermore, large contact area blunt impact could produce internal damage that is located far away from the immediate location of impact, namely at weak points (e.g., joints, transitions) along the load path transferring loads away from the impact location to surrounding internal structure. The damage modes and observations presented herein can serve to inform engineers from both design and maintenance perspectives, and can provide guidance on what damage modes to inspect for and where to search.

17. Key Words	18. Distribution Statement
Blunt impact, High energy, Non-visible damage, Damage resistance, Damage tolerance, Damage detectability, Composite fuselage structure, Shear tie, Testing, Dynamic loading	This document is available to the U.S. public through the National Technical Information Service (NTIS), Springfield, Virginia 22161. This document is also available from the Federal Aviation Administration William J. Hughes Technical Center at actlibrary.tc.faa.gov.

19. Security Classif. (of this report)	20. Security Classif. (of this page)	21. No. of Pages	22. Price
Unclassified	Unclassified	74	

ACKNOWLEDGEMENTS

This body of work would have been impossible to accomplish by the authors alone and by one single organization in isolation. Many people and companies were involved. Much important guiding information and feedback were provided over the years spanning this activity. This included participation in on-site meetings at UC San Diego, on-site visits at companies, and teleconference meetings at which valuable technical review and guidance were provided to the UC San Diego team. Furthermore, manufacturing assistance and autoclave access provided by local company San Diego Composites, as well as pre-preg composite materials provided by Cytec, were critical to this project. Deep gratitude is expressed to all the persons and organizations involved in contributing to the success of this project.

TABLE OF CONTENTS

LIST OF FIGURES

LIST OF TABLES

LIST OF ACRONYMS

DOF	Degree of freedom
GSE	Ground service equipment
HEWABI	High-energy wide-area blunt impact
LAX	Los Angeles International Airport
UAL	United Airlines

EXECUTIVE SUMMARY

Research has been conducted focused on understanding the formation of damage to composite structures when subjected to high-energy wide-area blunt impact (HEWABI) sources. Impact sources of interest are those acting over a wide area and potentially affecting multiple structural elements, but leaving little or no externally visible signs of the damage. This mainly involves heavy ground service equipment (GSE), such as belt loaders, cargo loaders, and catering trucks, which have soft rubber/elastomeric bumpers (also called spacers) mounted at protrusions where the GSE docks with the aircraft. Large carbon/epoxy composite test specimens having multiple stringers and frames were designed and fabricated. Conducted quasi-static and dynamic impact tests using rubber-bumper-faced indentors developed significant damage internally. Damage modes include internal components, such the shear ties, frames, and stringers.

Blunt impact tests have shown that significant internal damage can develop from HEWABI events, potentially with little to no external visually detectable indicators that a damage-producing event has occurred. Large-area contact with soft interface (bumper/spacer made of rubber/elastomeric materials) lowers contact stresses near the immediate location of impact, thereby reducing the chance of producing surface-visible skin cracks. Contact area during impact is a key parameter driving overall size (extent) of damage, as well as whether damage forms local to impact site or globally along the load paths transmitting contact forces into the surrounding internal structure. Therefore, a damage search following a HEWABI event should include inspection of the internal structure along these load paths (1 m length scale away) and locations around the aircraft at which GSE were closely docked (10 m length scale). High-strength composite external skins are able to deform significantly without cracking and permanent deformation to the skin. This is in contrast to ductile metal (e.g., aluminum alloy) skins, which yield and therefore have a higher chance of forming visually detectable residual dents. The use of such high-strength resilient composite skins presents a challenge to the visual detection-based paradigm of damage detection.

Future work recommendations include investigation of:

- Continuous shear-tie configurations
- Frame-to-floor joint connection stiffness effects.
- Glancing angle effects, particularly in the lower fuselage zone near the cargo floor plane.
- Establish general modeling capability for predicting observed failure modes—clear methodologies for how to predict HEWABI damage.
- Establish ability to predict thresholds of damage initiation (supports damage resistance).
- Relationship between global motion of the aircraft and local deformation/damage formation.

1. INTRODUCTION

Impact damage resulting from collisions of ground vehicles/equipment with aircraft structural components and from events such as hail and bird strikes is a significant source of damage to commercial aircraft that has the potential to go undetected. A commonly occurring blunt-impact threat comes from ground maintenance vehicles and service equipment (see figure 1).

Figure 1. Maintenance/service threat sources: ground vehicles, luggage carts, and cargo containers

This ground service equipment (GSE) accounts for a significant percentage of damage occurring to commercial transport aircraft. According to the International Air Transportation Association [1], 50% of major damage has been caused by GSE, and 60% of minor damage is caused by collision with ground vehicles/equipment, costing the industry billions of U.S. dollars per year. This occurs during cargo movement while loading the aircraft or docking of GSE around the aircraft doors. The areas in close proximity to the doorway openings, although reinforced with metallic “scuff plates” to protect against accidental damage, still incur damage beyond the coverage of the reinforcement. Figure 2 shows some examples of damage occurring at locations away from doors and a belt-loader interfacing an aircraft.

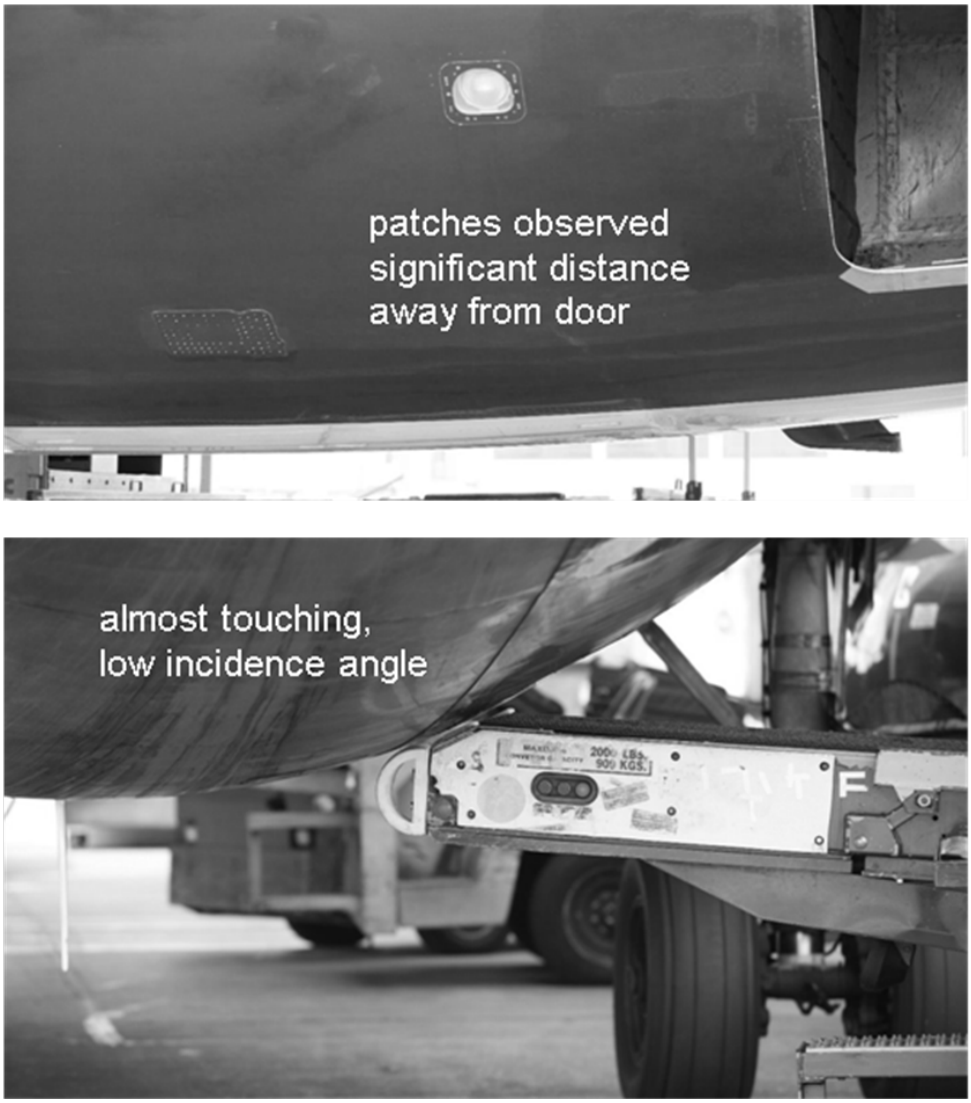

Figure 2. Examples of damage occurring in acreage of aircraft (i.e., away from doors) and interaction between belt-loader and fuselage of Boeing 737.

With new all-composite fuselage transport aircraft coming into service, significantly more composite skin surface area is exposed to such impacts. To address the difficulties that exist in being able to detect the damage resulting from blunt impact and to aid in assessing its effect on structural performance, focused investigation on the development of GSE-induced impact damage has been conducted at UC-San Diego.

Of particular interest is damage that can be difficult to visually detect from the exterior but could be extensive below the skin's outer surface. Extensive subsurface damage (typically delamination, backside fiber failure, or stringer separation) usually forms when impacts occur at levels just exceeding the amount needed to initiate failure [2 and 3]. This level is referred to as the failure threshold energy. Additionally, damage from blunt impacts to internal stiffeners can be extensive, including frames, shear ties, and disbonding between the stiffener and the skin. Of critical concern

is whether such extensive damage can result in the structure losing ultimate and even-limit load capability.

Blunt impacts can be defined as impact sources that can affect large areas or multiple structural elements, although potentially leaving little or no externally visibly detectable signs of damage. Blunt impacts come from a variety of sources and can involve a wide range of energy levels. The focus of this report is on the GSE impact onto aircraft fuselage-type structure. Such GSE, although moving at very low velocities of often less than 0.5 m/s, involve very high energy because of their high masses. Therefore, this category of impact threat is referred to as high-energy wide-area blunt impact (HEWABI). Various example GSE blunt impact sources are shown in figure 3 with portions of the aircraft for which such threats typically occur: mainly the side and lower facing surfaces of the aircraft.

Figure 3. Example of GSE blunt impact sources

The primary objective of the UC-San Diego HEWABI research was to assess the damage resistance, and the extent of damage formed, of composite structures subjected to impact by wide-area blunt sources such as ground vehicles. This included developing an understanding of failure modes, internal stresses, and relationships between loading situations and varying geometric (and stiffness) properties of the indentor. This was achieved by a combination of experimental observation of the evolution of damage modes (failure history) for a series of large-sized test specimens and the determination of the spatial extent of damage possible within these specimens. Specific interest was to find conditions that directly relate to widespread internal structural damage with little to no visual detectability. This was especially important for GSE with rubber bumper

materials that soften the contact-interaction with aircraft structure, in combination with composites that did not dent easily unless subjected to locally concentrated impact forces. Large-scale blunt impact experimental activities reported on herein were focused on establishing a basic understanding of key failure modes, how these were excited, and the establishment of a well-defined experimental database measuring structural response and failure sequences development. In addition to assessing the mechanisms of how blunt impact damage forms, these data intendedly served as validation sources supporting the development of modeling methodology and simulation tools for predicting HEWABI damage.

2. GROUND OBSERVATIONS

As part of the FAA-funded program on blunt impact, interactions with United Airlines (UAL) permitted ground observation of GSE in close proximity to transport aircraft. This observation occurred on March 19, 2009 at Los Angeles International Airport (LAX), UAL Gates 66, 72, 73, 75A&B, 76, and the maintenance hangar area. UC-San Diego persons were escorted by UAL engineering and maintenance staff. The purpose of this activity was to make first-hand observations and document the interactions between GSE and aircraft between flights. From the observations made, a quantitative understanding of potential impact sources and scenarios was obtained. Measurements, photos, and videos were taken of GSE, typical bumpers, and potential contact surfaces and locations to scale dimensions and the speeds of GSE. Docking practices for a variety of aircrafts were observed. Approach speeds and general near-aircraft movement of ground vehicles were also observed.

Per discussions with UAL personnel, it was conveyed that damage to aircraft often results from cargo movement while loading the aircraft or docking of the GSE and passenger bridge around the aircraft doors. Areas in close proximity of the doorway openings are therefore typically reinforced to protect from this type of anticipated damage. Other events can occur (less common), such as maintenance equipment or other unattended GSE blown into the aircraft, or the aircraft settling down onto equipment during the fueling and passenger-loading processes. These scenarios could cause damage further away from the reinforced door areas. Additionally, damage far away (i.e., meters) from the doors can commonly be observed to exist as well (see figure 2), created by undefined sources.

The aircraft observed at LAX included: The Boeing Company models 737, 747, 757, 767, and Airbus 320. Different aircraft geometries and sizes influence the possible impact sources. Smaller aircraft, such as the B737, have a shorter turnaround time between flights, often as low as 35 minutes, therefore, operations around these aircraft can be more rushed. There is sometimes limited space around smaller aircraft (if smaller gate spacing exists), leading to more concentrated GSE traffic levels in tight proximity of one another. During the UC-San Diego's observation activity, one single B737 was observed to be serviced by GSE for fuel, luggage, catering, and lavatory, all simultaneously. A smaller aircraft, like the B737 fuselage, is at high risk of direct contact with the GSE because of its low height from the ground (e.g., see belt loader with B737 in figure 2). GSE impact could involve more than one piece of equipment. For example, one possible source of impact described by ground operations persons is a luggage-towing vehicle driving too fast as it approaches to unload, and accidentally colliding with the properly parked belt loader, which then impacts the aircraft.

There is a different set of threats associated with larger aircraft, such as the B747 and B767. The angle of approach for docking (i.e., for the catering truck) is more difficult toward the tail of the aircraft than for the smaller aircraft because of curvature toward the tail (see figure 4). However, the bottom of the fuselage of a large aircraft is much higher, thereby eliminating contact from sources, such as vehicles and luggage carts, driving by. Scraping damage to the wing-to-body fairing on the B747 (see figure 4) is reported as common during the lifting of the catering truck platform to access the forward door.

(a) patches surrounding door **(b) belt loader and difficult approach angle**

(c) wing-to-body fairing

Figure 4. Docking at difficult locations: tail area and near wing fairing: (a) patches surrounding door, (b) belt loader and difficult approach angle, and (c) wing-to-body fairing

The corners and extremities of GSE usually have a soft material bumper (also called spacer) fitted to them, particularly at the locations where the equipment is intended to come in contact with the

aircraft. These materials are typically rubber/elastomer. Table 1 describes typical bumpers observed on various GSE, together with the photos shown in figure 5.

Table 1. Description of bumpers on GSE

GSE Type	Bumper Type	Approx. Radius (in.)	Width (in.)	Material
Belt loader	See Fig. 2.2a	3.5	3.25	Stiff rubber
Catering truck	See Fig. 2.2b	3.5	Width of GSE	Rubber tube
Large cargo loader	See Fig. 2.2c	2–2.5	Width of GSE	Rubber tube
Luggage container	See Fig. 2.2d	2.5	Corner	Stiff rubber
Luggage container	See Fig. 2.2e	2.5	Corner, 4.5	Stiff rubber

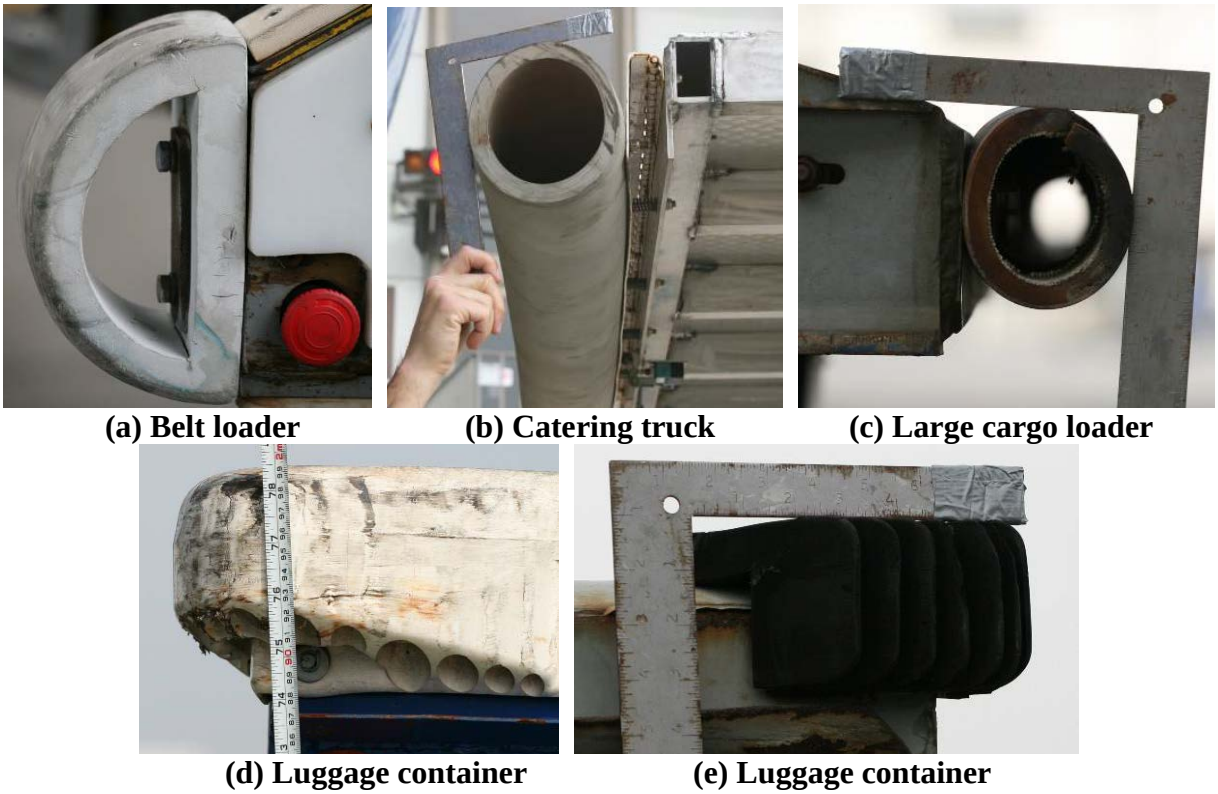

(a) Belt loader **(b) Catering truck** **(c) Large cargo loader**

(d) Luggage container **(e) Luggage container**

Figure 5. Typical bumpers for GSE and luggage containers: (a) belt loader, (b) catering truck, (c) large cargo loader, (d) luggage container, and (e) luggage container.

Velocity of GSE approaching the aircraft is a key parameter governing blunt impact. Based on the analysis of videos documenting GSE approach, an understanding of the typical velocity possible in near proximity to aircraft was quantified. Figure 6 shows still images extracted from a video of a belt loading approaching an aircraft. The video analysis plotted the velocity of the GSE versus distance relative to a full stop (position = 0). Within a 10-cm distance of a full stop, the GSE was still moving at a velocity of 0.5 m/s (approximately 1 mile per hour). Because the TUG belt loader depicted a weight of approximately 3030 kg, the total kinetic energy of this large moving body was more than 300 J. At 1 m/s speed (~2 miles per hour), the GSE would have ~1500 J kinetic

energy. It should be noted that the belt loader of the GSE in figure 6 was not deployed in the “up” position while approaching near the aircraft; therefore, approach speeds in this case were likely higher than when actually docking. The second example shown in figure 7 provides the valuable viewpoint of GSE docking with an aircraft. Here a catering truck approached and first came to a full stop before more slowly moving forward, very close to the aircraft. This was executed by the driver following visual-based (hand) instructions given by a person on the ground. Even during the slower docking stage when the GSE was nudging forward, the GSE was still moving at 0.25 m/s (just more than ~1/2 mile per hour), corresponding to more than 300 J kinetic energy.

These examples provide realistic velocity of GSE in normal operation around aircraft. Slower speeds can exist in case of aircraft settling onto equipment as passenger, cargo, and fuel is loaded. Faster speeds are also possible, in cases of negligent GSE operation resulting in true collisions with the aircraft;, however, events involving these faster speeds are often more likely to be detected relative to slower events, particularly those occurring during normal operation of GSE near the aircraft.

Finally, since there are often multiple GSE docked simultaneously around an aircraft, when a severe high- energy impact event occurs, the whole aircraft would subsequently exhibit global motion, which can then result in contact-impact with the other surrounding GSE. Therefore, all locations in which GSE are docked in close proximity to the aircraft are potential locations of blunt impact damage. These locations should also be inspected following a HEWABI event.

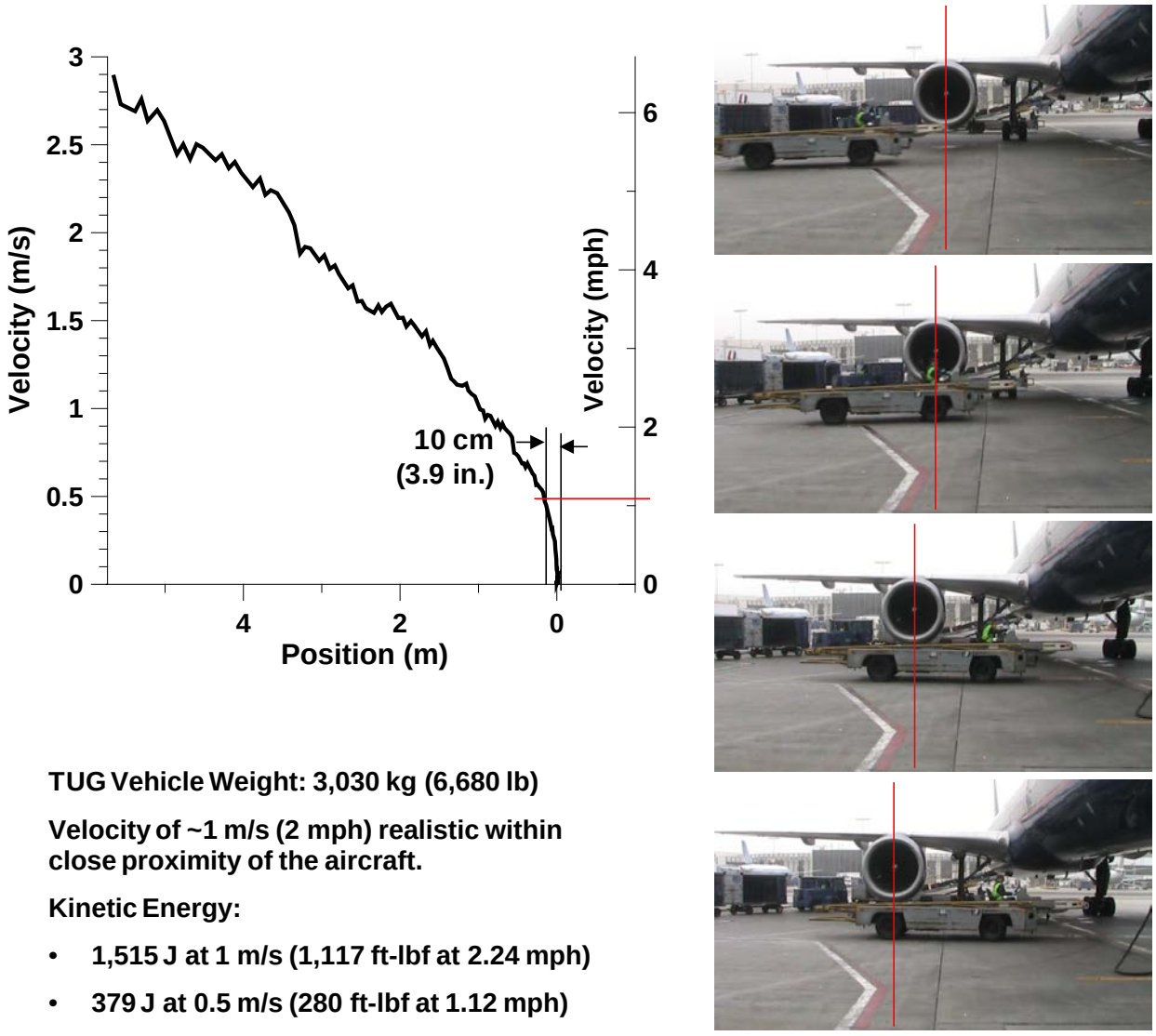

TUG Vehicle Weight: 3,030 kg (6,680 lb)

Velocity of ~1 m/s (2 mph) realistic within close proximity of the aircraft.

Kinetic Energy:

- **1,515 J at 1 m/s (1,117 ft-lbf at 2.24 mph)**
- **379 J at 0.5 m/s (280 ft-lbf at 1.12 mph)**

Figure 6. TUG belt loader approach and velocity

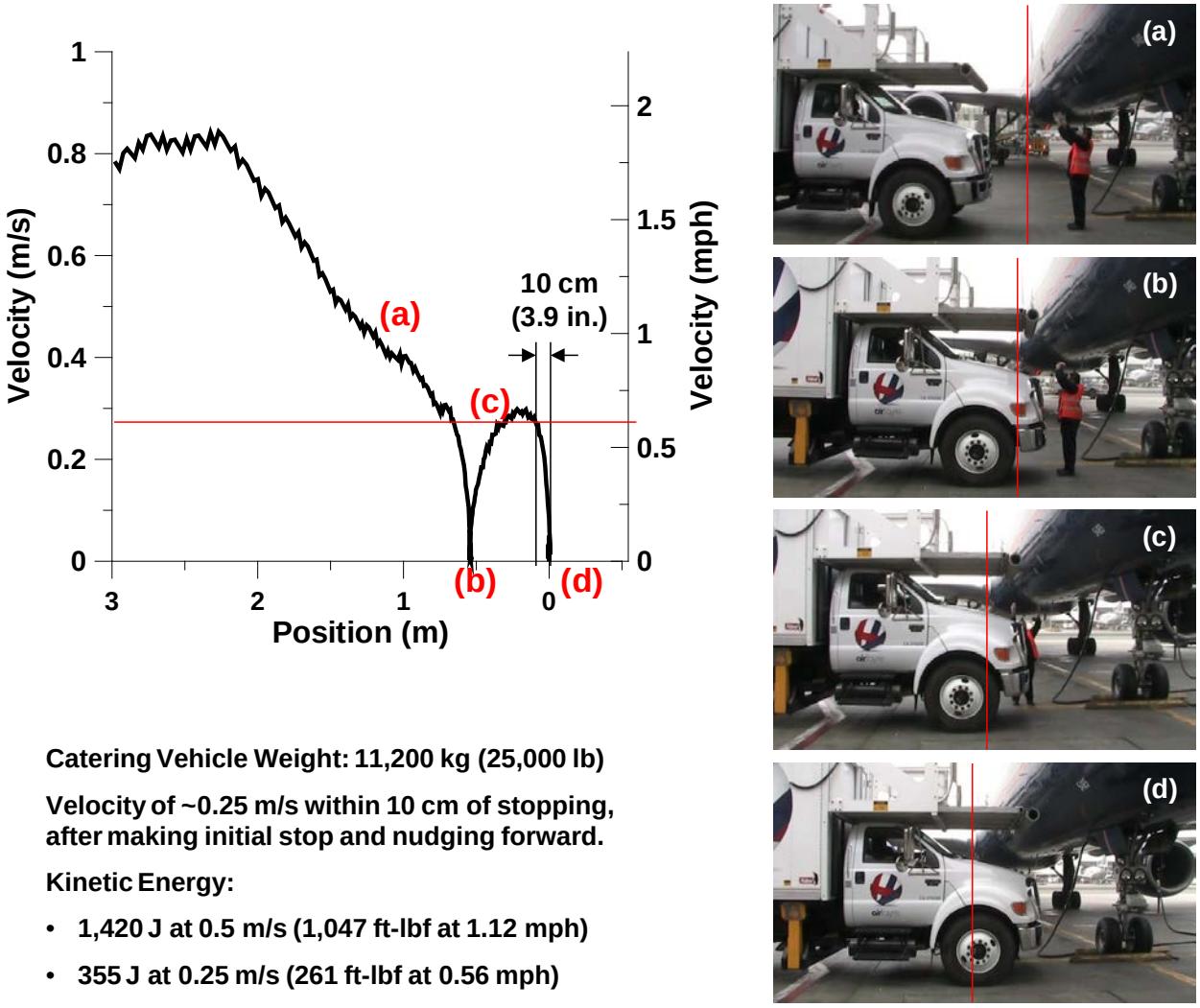

Figure 7. Catering vehicle approach and velocity

These examples provide realistic velocity of GSE in normal operation around aircraft. Slower speeds can exist in case of aircraft settling onto equipment as passengers, cargo, and fuel are loaded. Faster speeds are also possible in cases of negligent GSE operation resulting in true collisions with the aircraft; however, events involving these faster speeds are often more likely to be detected relative to slower events, particularly those occurring during normal operation of GSE near the aircraft.

Finally, because multiple GSE are often docked simultaneously around an aircraft, when a severe high-energy impact event occurs, the whole aircraft would subsequently exhibit global motion, which can then result in contact-impact with the other surrounding GSE. Therefore, all locations in which GSE are docked in close proximity to the aircraft are potential locations of blunt impact damage. These locations should also be inspected following a HEWABI event.

3. UC-SAN DIEGO PANEL TEST SPECIMENS

3.1 SPECIMEN DESCRIPTION

Two types of panel specimens were devised with the guidance from industry over the course of two workshop meetings held onsite at UC-San Diego. The first configuration (specimen ID series: FrameXX), shown in figure 8, is primarily focused on damage development to the circumferential frame members and the shear ties connection to the skins.

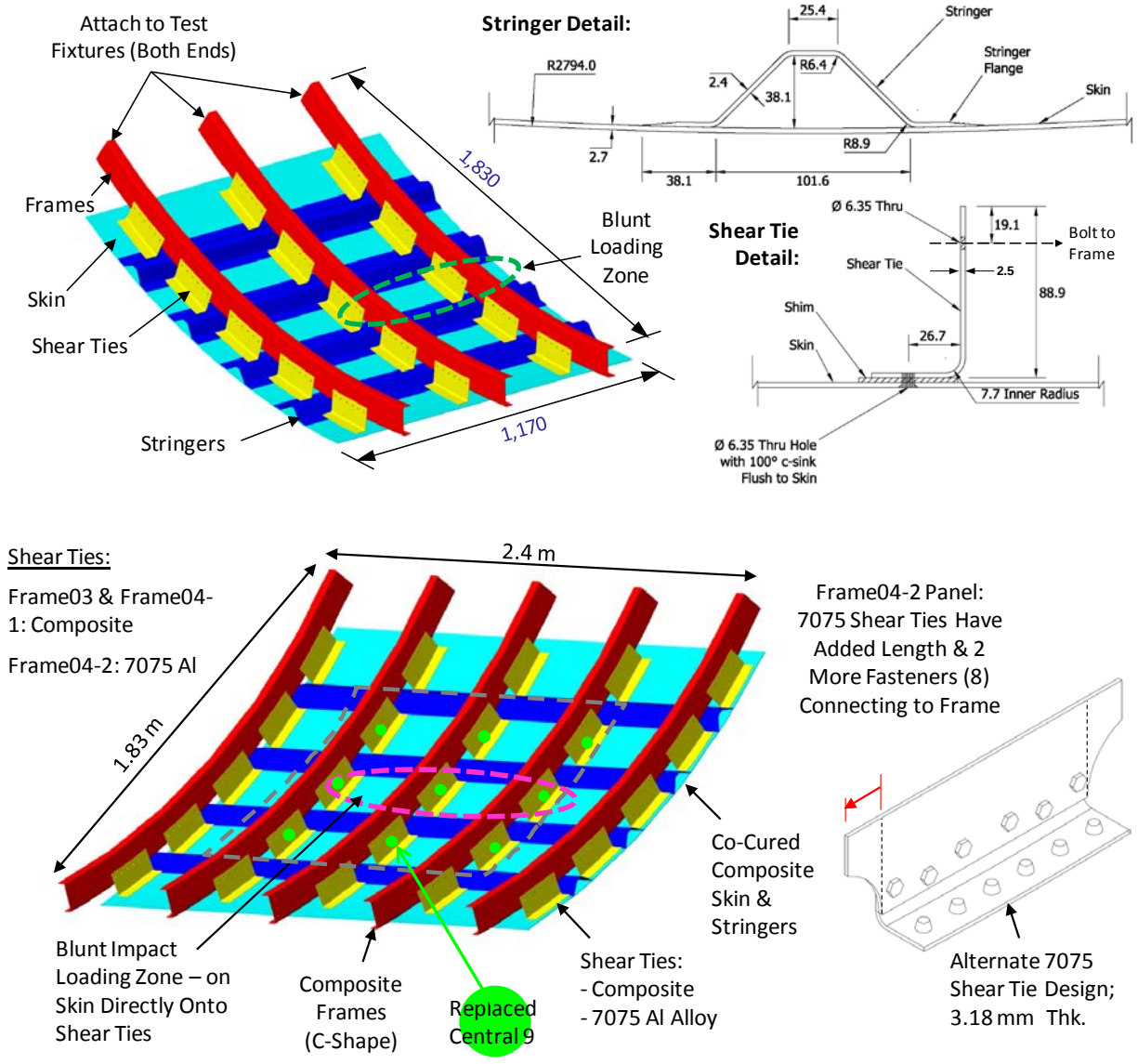

Figure 8. Frame focused test specimen (series ID: FrameXX); C-shaped frames have overall section dimensions 108 x 32 mm with 2.9 and 2.5 mm thick flanges and web, respectively. All dimensions are mm unless otherwise noted

These three-frame and five-frame panels represent both the steady-state zone, as depicted in figure 9, and the transitional zone, where the indentor terminates, thereby producing biaxial bending at that location. The three-frame panels were tested quasi-statically with loading across two of the frames, whereas the five-frame panels were tested dynamically with loading applied across the central three frames (see figure 9). Only the five-frame panel results are described in this report (specimen IDs Frame03, Frame04-1, and Frame04-2) because the three-frame panels (specimen IDs Frame01 and Frame02) were quasi-statically loaded as a basic study in preparation for the dynamic impact loading of the five-frame panels.

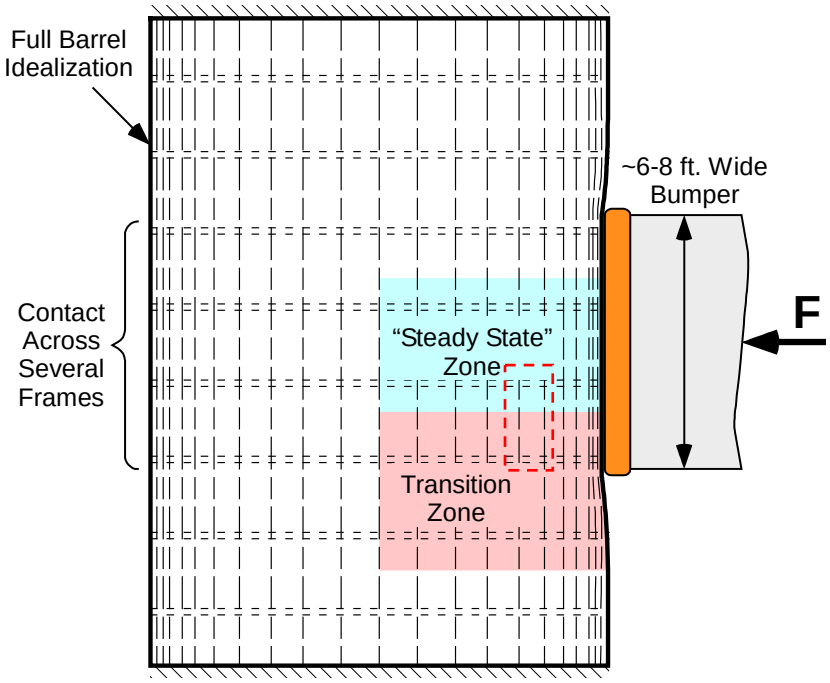

Figure 9. Deformation zones for GSE bumper impact onto full barrel

The second specimen type, shown in figure 10, is focused on damage formation to the stringers and their connection to the skins (i.e., representing localized—not line load—impacts occurring between frames). Such impacts would occur from GSE corners or narrow-width bumpers similar to those found on belt loaders (see table 1 and figure 5).

Figure 10. Stringer focused test specimen (series ID: StringerXX); 2-stringer panel not shown would be impacted on skin between stringers

A summary of blunt-impact/indentation tests conducted under this program is shown in table 2, which indicates the specimen configurations and testing conditions for both specimen types. This includes smaller “StringerXX” and larger “FrameXX” panels.

Table 2 also includes a summary of the peak forces, maximum indentation, and resulting damage modes, and whether visible damage resulted from the test. Details of these tests are found in section 4, Experimental Results.

Table 2. GSE blunt-impact tests summary

Specimen ID	Panel Config	Loading Details	Intermediate Failure Modes	Final Failure Mode	Visible?	Max Load (kN)	Max Indent (mm)
Frame01	4 Stringers, 3 Frames	Long Cyl. Bumper Spans 2 Frames, Between Stringers, Q-Static	Shear Ties Crush, Stringer Sever & Flange Delam	Frame Crack	N	57.4 (28.7/Frame)	75.5
Frame02	5 Stringers, 3 Frames	Long Cyl. Bumper Spans 2 Frames, at Stringer, Q-Static	Shear Ties Crush, Stringer Sever & Flange Delam, Skin Crack	Frame Crack	Y	71.0 (35.5/Frame)	55.9
Frame03	4 Stringers, 5 Frames	Long Cyl. Bumper Spans 3 Frames, Between Stringers, *Dynamic*	Shear Ties Crush (Qnty 3) & Bending Failure (Qnty 6)	3 Frames Severed, Each @ 2 Locations	N	74.1 (24.7/Frame)	90.9
Frame04	4 Stringers, 5 Frames	Long Cyl. Bumper Spans 3 Frames, Between Stringers, *Dynamic*	Shear-Thru Failure of Frame (Qnty 3)	3 Frames Severed by Shear Ties	N	126	90
Stringer00	3 Stringers	R3" Alum. Over Stringer, Q-Static	Skin Delamination	Local Skin Penetration	Y	30.7	25.3
Stringer01	2 Stringers	R3' Alum. On Skin Between Stringers, Q-Static	Skin Delamination	Local Skin Penetration	Y	26.7	21.8
Stringer02	2 Stringers	D-Bumper on Skin Between Stringers, Q-Static	Skin-Stringer Delamination of Each Adjacent Stringer	Extensive Stringer-Skin Delamination	N	61.7	39.5
Stringer03	3 Stringers	D-Bumper Over Stringer, Q-Static	Stringer Radius Cracks Under Indentor	Extensive Stringer-Skin Delamination	Y	61.6	~48.5
Stringer04	3 Stringers	D-Bumper on Stringer Flange, Q-Static	Stringer Radius Cracks Under Indentor	Extensive Stringer-Skin Delamination	Y	78.2	~44.2
Stringer05	2 Stringers	D-Bumper on Skin Between Stringers, *Dynamic*	Stringer-Skin Delamination (Just Before Final Failure)	Stringer Flange & Rad. Failure & Fracture, Delamination	Y	67.0	n/a
Stringer06	3 Stringers	D-Bumper Over Stringer, *Dynamic*	Stringer-Skin Delamination (Just Before Final Failure)	Stringer Radius Failure & Fracture, Delamination	Y	57.4	n/a

The number of stringers on each panel type defines whether the impact location was directly over a stringer or on the skin bay between stringers (which are spaced 305 mm apart), as shown in figures 11 and 12. For the FrameXX panels, only panel Frame02 had five stringers with loading directly onto the stringer location, whereas all other FrameXX panels had four stringers with loading on the skin bay, as shown in figure 12. For select StringerXX panels, a rigid hard aluminum indentor was used to load panels quasi-statically (see figure 13). An OEM rubber bumper, which was purchased from a major company making GSE (TUG), used to load the StringerXX panels at their center location, as shown in figure 14. The indentor used to load the frame specimen simulates a full-width bumper contact (e.g., from heavy cargo loader or catering truck) and is shown in figures 12 and 15.

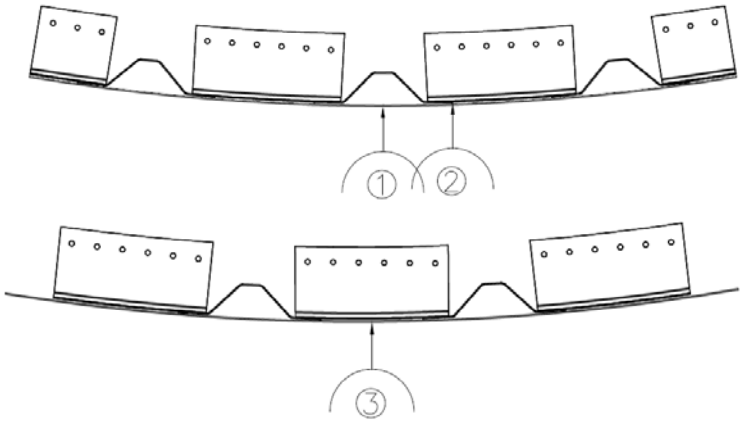

Figure 11. Stringer panel impact locations for 2-stringer and 3-stringer panels

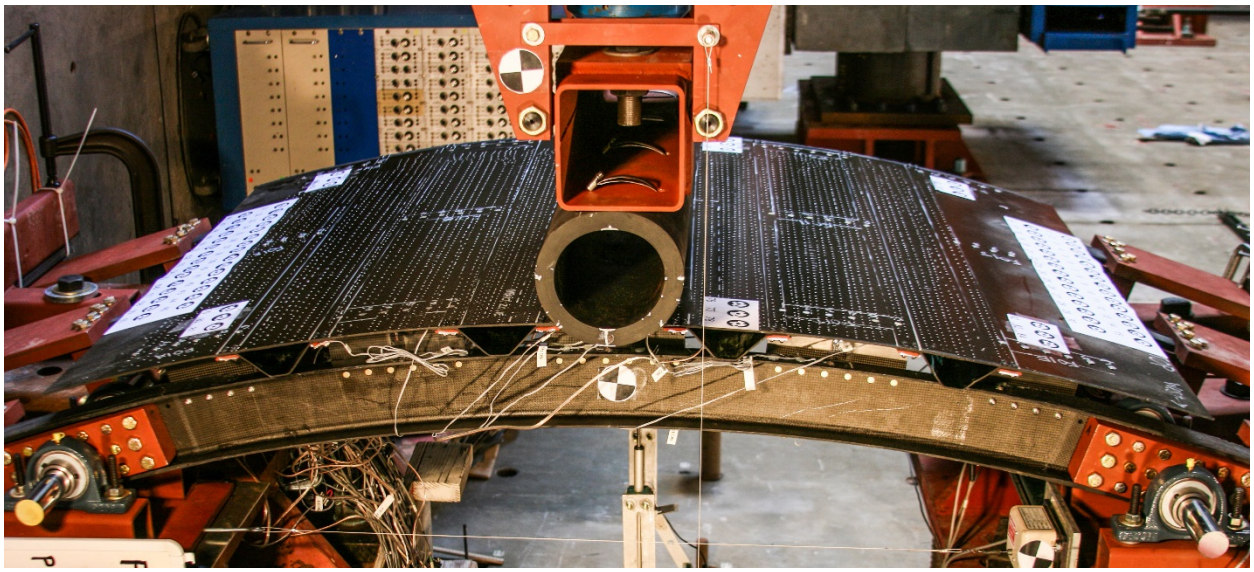

Figure 12. Impact location for 4-frame panels contacting skin bay between stringers (specimen IDs Frame01, 03, and 04); impact location for 5-frame panels located directly above stringer (only specimen ID Frame02)

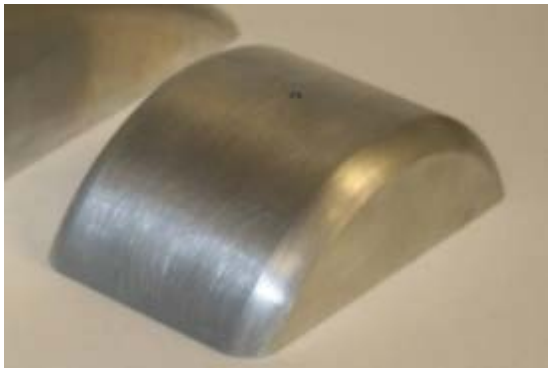

Figure 13. Aluminum “rigid” indentor for stringer specimen tests having 76.2 mm radius

Figure 14. OEM rubber bumper for stringer specimen tests

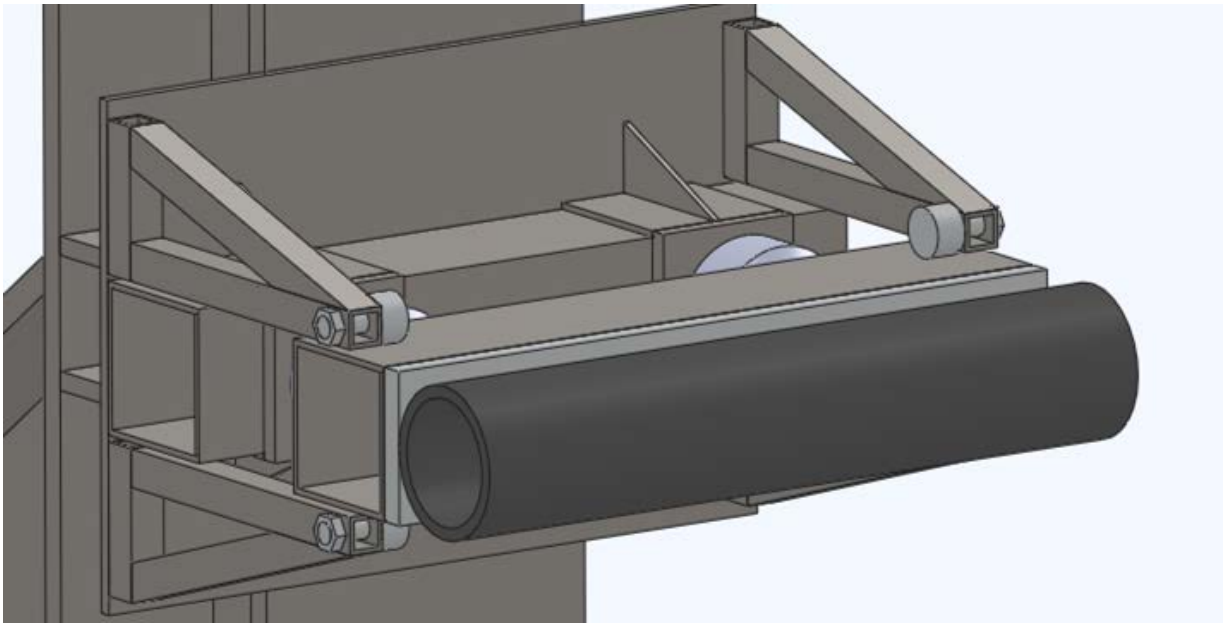

Figure 15. Rubber bumper for frame specimen tests; bumper outer diameter 178 mm, wall thickness 25 mm.

3.2 MANUFACTURING

All the test specimens were fabricated by UC-San Diego with consultation from local company San Diego Composites. A documentation system of material out-time tracking and ply layup tables with check-off sheets was used to control quality of parts production. Specimen materials were carbon fiber and toughened epoxy matrix (reflecting current aerospace fuselage materials) provided by industrial partner Cytec Engineered Materials (now Solvay). Specifically, these materials were X840 unidirectional tape, and X840 3k and X840 6k woven fabrics.

For both stringer and frame specimens, the stringers and shims (spacers to ensure a constant thickness to bolt shear ties to skin) were co-cured to the skin. Layup for all parts was done by hand at UC-San Diego, then transported to San Diego Composites for autoclave cure.

The cure cycle was as follows:

- Apply 22 in Hg vacuum.
- Apply 85–100 psi, do not vent vac.
- Heat-up to 355 +/- 10 °F at 1-5 °F/min.
- Hold 120–180 minutes at 355 +/- 10 °F.
- Cool to < 140 °F at 5 °F/min max.

The skin layup was $[0/45/90/-45]_{2s}$ with a single layer of 3K plain weave fabric on each side (2.7 mm thick), and the stringers layups were $[0/45/-45/90/45/-45/0]_s$ (2.4 mm thick). For both the stringer and skin, the 0° direction was longitudinal along the stringer's axis direction. The frames and shear ties were all-fabric 6K plain weave for increased drapability into compound curved regions of the tools. The shear ties had a layup sequence of $[45/0]_{3s}$ (2.5 mm thick), and the frames had the same layup sequence, with an additional two 0° (woven) layers added to the caps for increased bending rigidity (caps 2.9 mm thick). For these parts, the 0° direction was along the frame main length. The shear ties and frames were a bolted assembly using 6.35 mm shank (1/4 in. diameter) HI-LOK™ fasteners. Finished parts are shown in figures 10 and 16–18.

Figure 16. Three-frame specimen without frames or shear ties; approximate overall dimensions 1.83 m in curved direction by 1.2 m in stringer direction

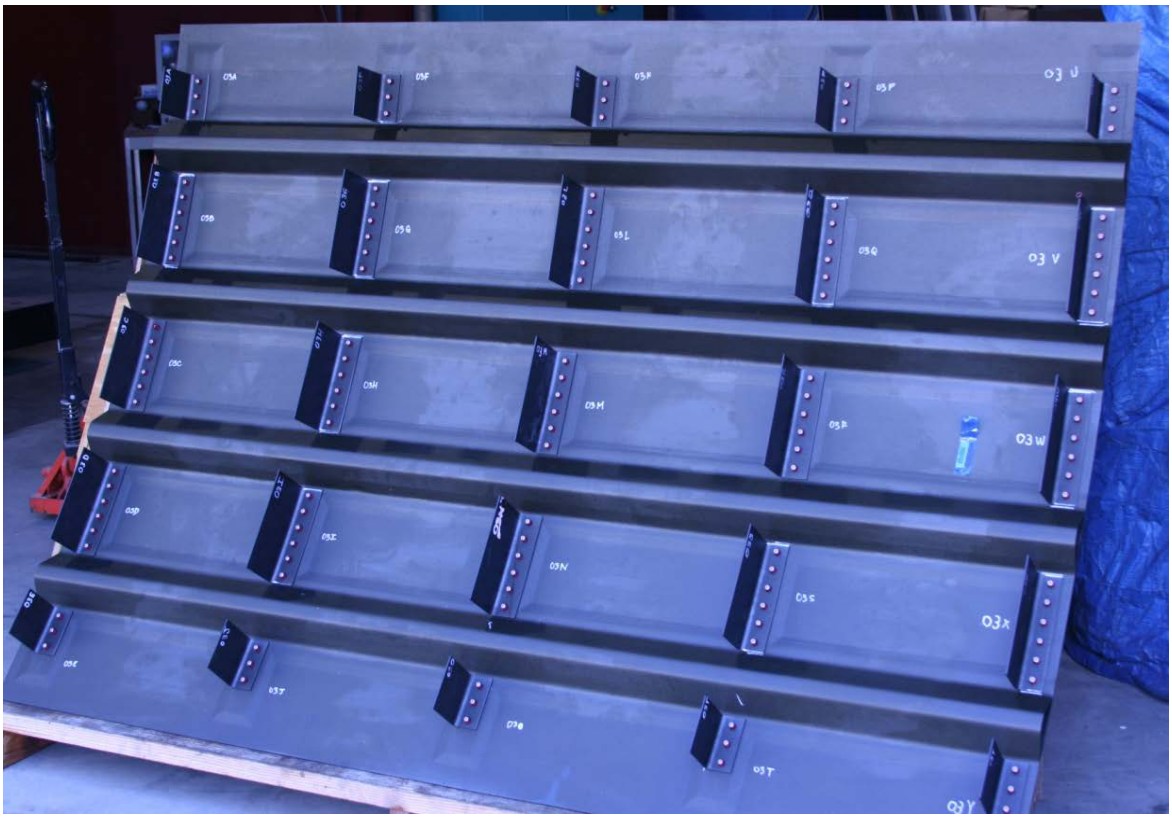

Figure 17. Five-frame specimen with shear ties mounted but no frames; overall dimensions 1.83 m in curved direction by 2.4 m in stringer direction

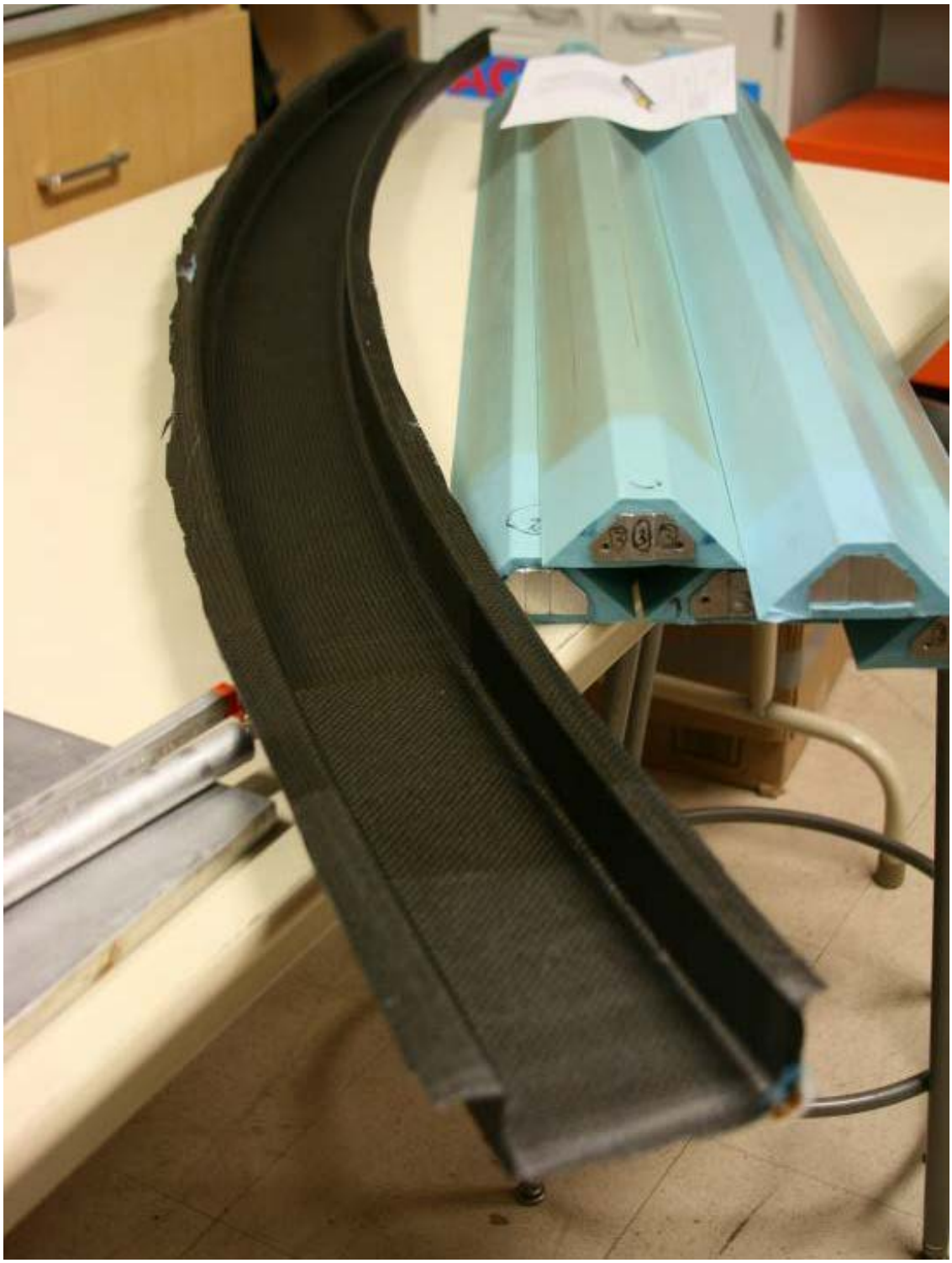

Figure 18. Untrimmed C-frame; stringer internal silicone molds

An important detail of the specimens was the stringer-to-skin corner geometry. Manufacturing trial studies were used to determine the best way to control this geometry and to ensure that the desired radius was maintained in this location and that the geometry was consistently produced for each

specimen in all stringers. This was important because one of the key anticipated failure modes was delamination of the stringer flanges from the panel skin. The corner detail geometry shown in figure 19 was repeatedly achieved by adding a step to the corner of the stringer molds and including folded 0° unidirectional tape to fill the corner volume (see center detail in figure 19).

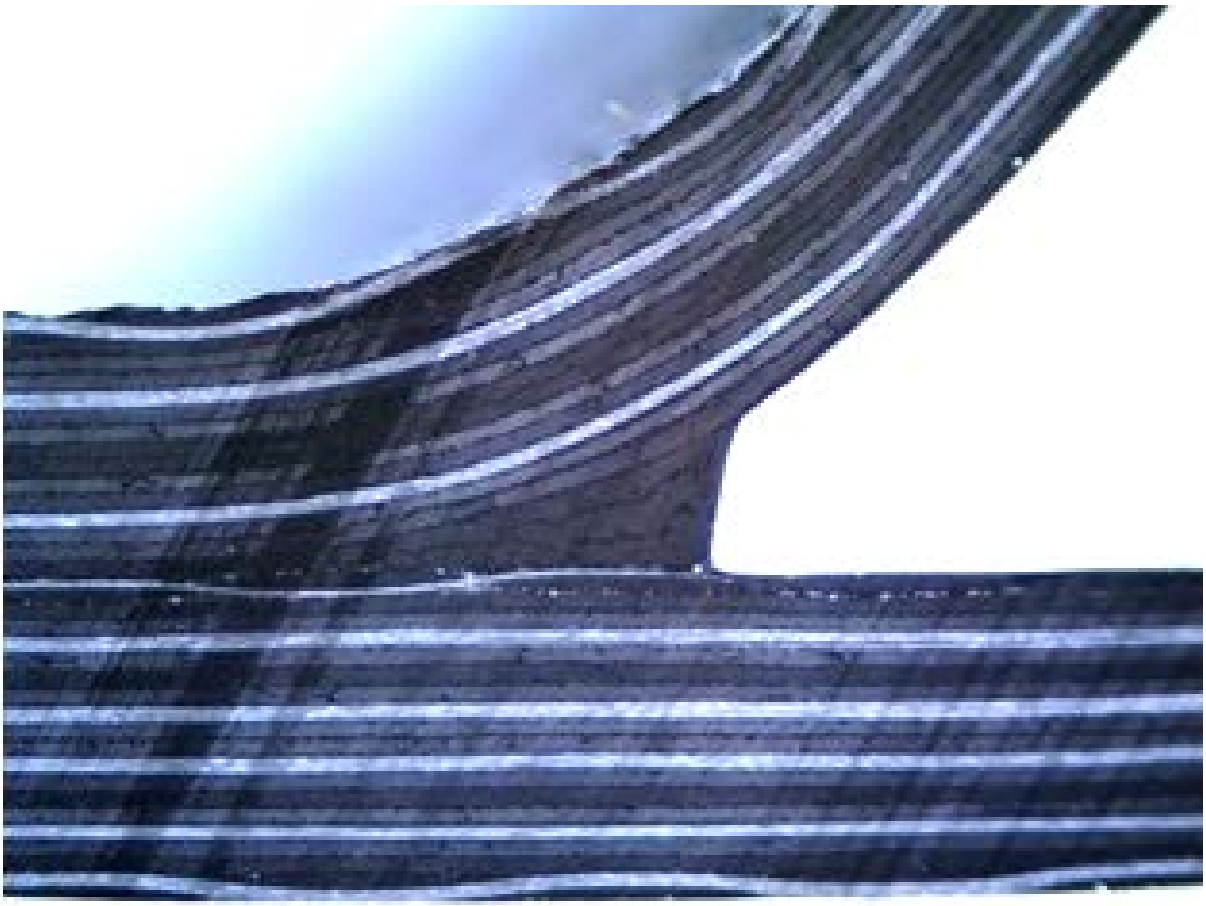

Figure 19. Corner detail of stringer-to-skin connection

3.2.1 Manufacturing Challenges

It should be noted that the manufacturing activity had been greatly challenging, with many setbacks in tooling acquisition (supplier manufacturing errors) and a large number of person-hours of labor required to cut plies and conduct layup for each specimen. This component of the project was a source of much delay in schedule. The benefit, however, was that the specimen, being 100% designed and manufactured by UC-San Diego, had no associated restrictions affecting the public dissemination of the specimen details and test results.

4. EXPERIMENTAL RESULTS

4.1 STRINGERXX SPECIMENS

Detailed reports of the two-stringer panels experiments (i.e., specimen IDs Stringer01, 02, and 05) are presented to illustrate the general damage modes observed. These two-stringer panel specimens were loaded on the skin bay between the reinforcing stringers. Stringer01 and Stringer02 were quasi-statically indented with the aluminum indenter and rubber bumper, respectively. The effect of the indenter bluntness was determined by comparing the resulting damage and load versus displacement curves. Stringer05 was dynamically loaded with the rubber bumper. The effects of loading speed were determined by comparing Stringer05 to Stringer02 results. Next, the results from the three-stringer panels (i.e., Stringer00, 03, and 06) are presented. The three-stringer panel specimens were loaded directly onto the middle stringer, with load specifically applied onto the short span of skin connecting between the stringer walls. The effect of loading locations (on stringer or on skin bay) is determined by comparing the two-stringer panel results to the three-stringer panel results.

4.1.1 Stringer01 Experimental Results

Stringer01 was quasi-statically indented with the 76.2 mm radius aluminum indenter (see figure 13) on the skin bay between the stringers (i.e., not directly onto stringer). Figure 20 shows the panel surface during contact with the indenter. Because the aluminum indenter was essentially rigid compared with the carbon fiber skin, the skin deformed locally around the indenter. The contact stresses were the highest at the small-radius edges of the indenter (see figure 20) leading to damage initiation at these locations. The Stringer01 panel was indented over four progressively increasing loading cycles. Figure 21 shows the contact force versus indentation plots for the load cycles. During the first loading, popping sounds were heard, but no detectable damage was found. During the second loading, local skin delamination damage was detected underneath the indenter at a load of 13.34 kN and an indentation displacement of 14.73 mm. The delaminations were oval-shaped. Their locations coincided with indenter's small-radius edges (see arrows in figure 20). During the third loading, small clicking sounds were heard after 13.79 kN. The test continued until the next significant failure event occurred at 22.83 kN and an indentation of 20.57 mm. The damage mode was local skin delamination growth under the indenter. The specimen was then reloaded for a fourth loading, during which a loud crack noise was heard at 26.71 kN and 21.84 mm indentation displacement. Local skin penetration damage was generated (see figures 22 and 23). The hatched zones also shown in figure 23 were the delamination zones mapped out with ultrasonic A-scan after loading cycles 2 and 3.

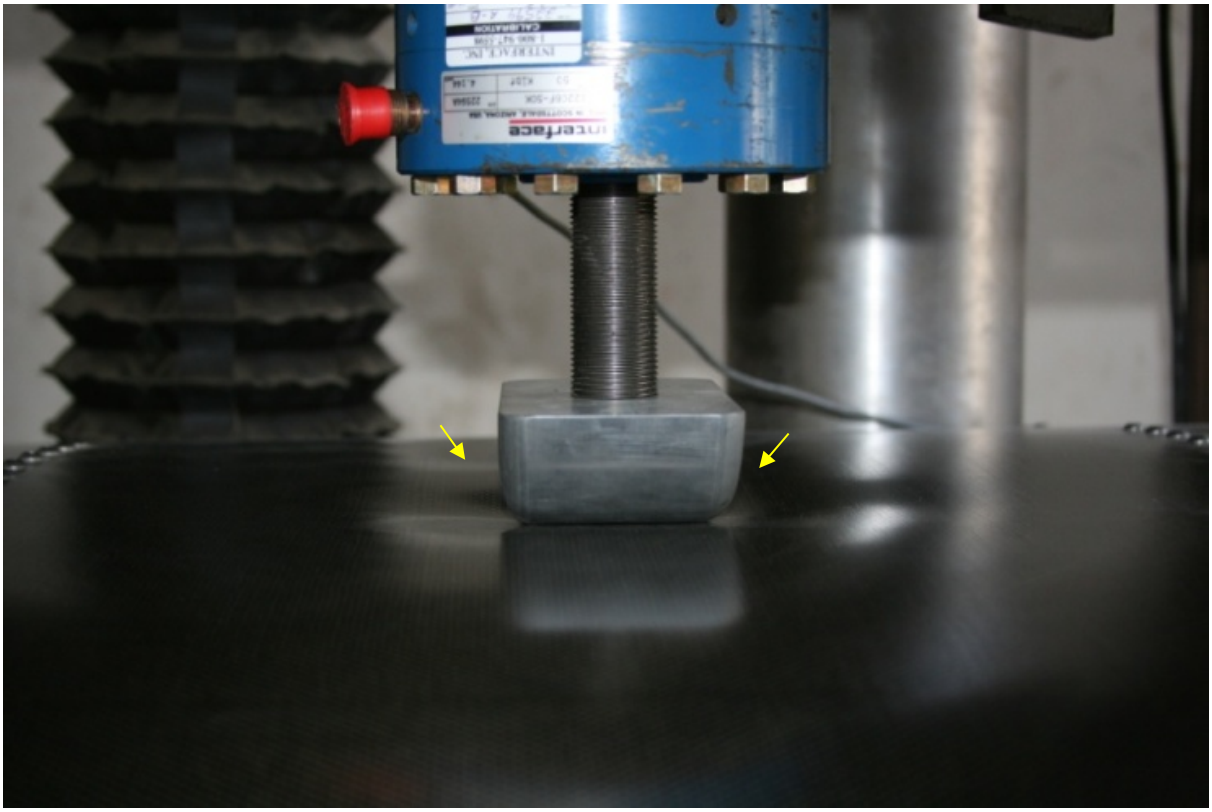

Figure 20. Contact between the aluminum indenter and Stringer01 external skin; arrows indicate highest stress locations

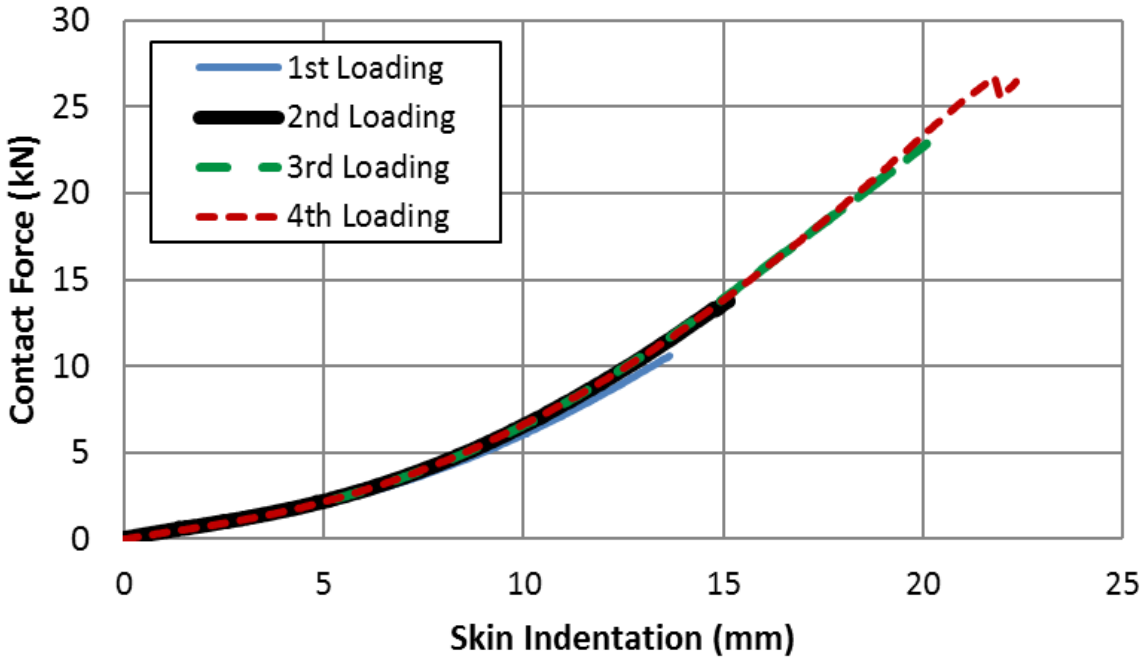

Figure 21. Stringer01 contact force vs. skin indentation plots

Figure 22. Stringer01 local skin penetration

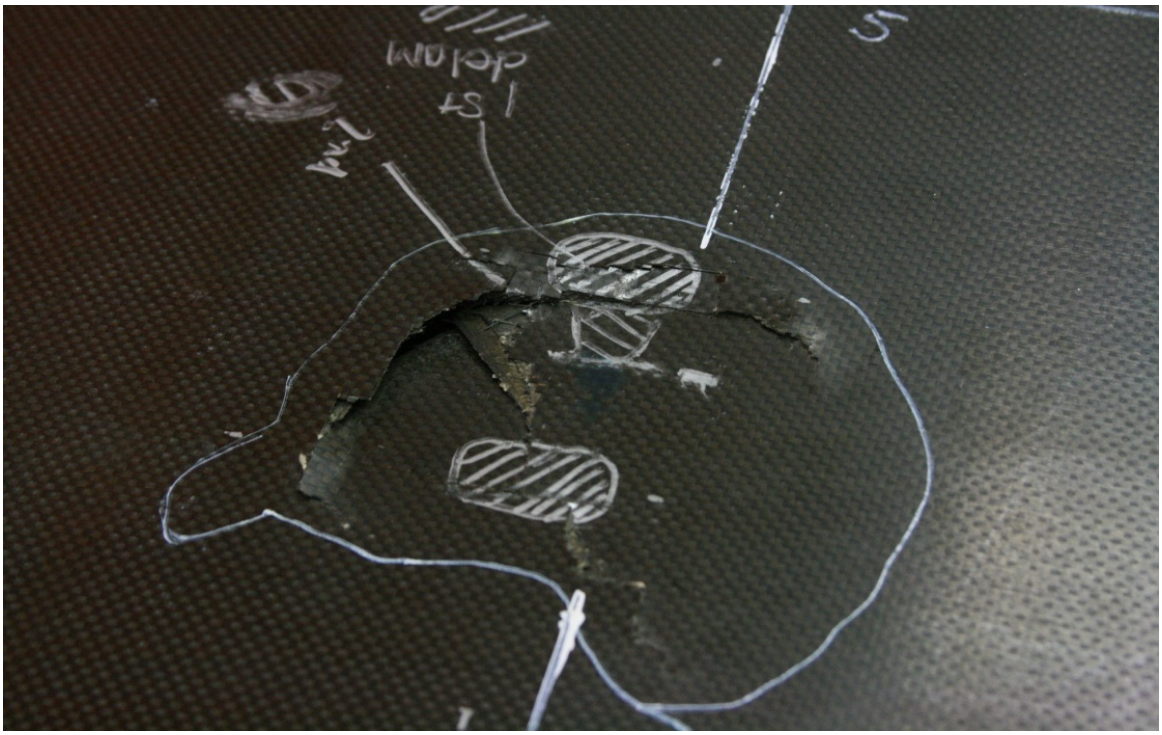

Figure 23. Stringer01 skin penetration and delamination damage

4.1.2 Stringer02 Experimental Results

Stringer02 was quasi-statically indented with the TUG D-shaped rubber bumper on the panel's skin between the stringers. Figure 24 shows the highly deformed bumper contacting with the skin of panel Stringer02 (see undeformed bumper shown in figure 14). In this case, the contact stresses were reduced because of flattening of the hyperelastic behavior of the rubber; therefore, local skin delamination was not found. The Stringer02 panel was quasi-statically loaded five times at increasing load levels under displacement control.

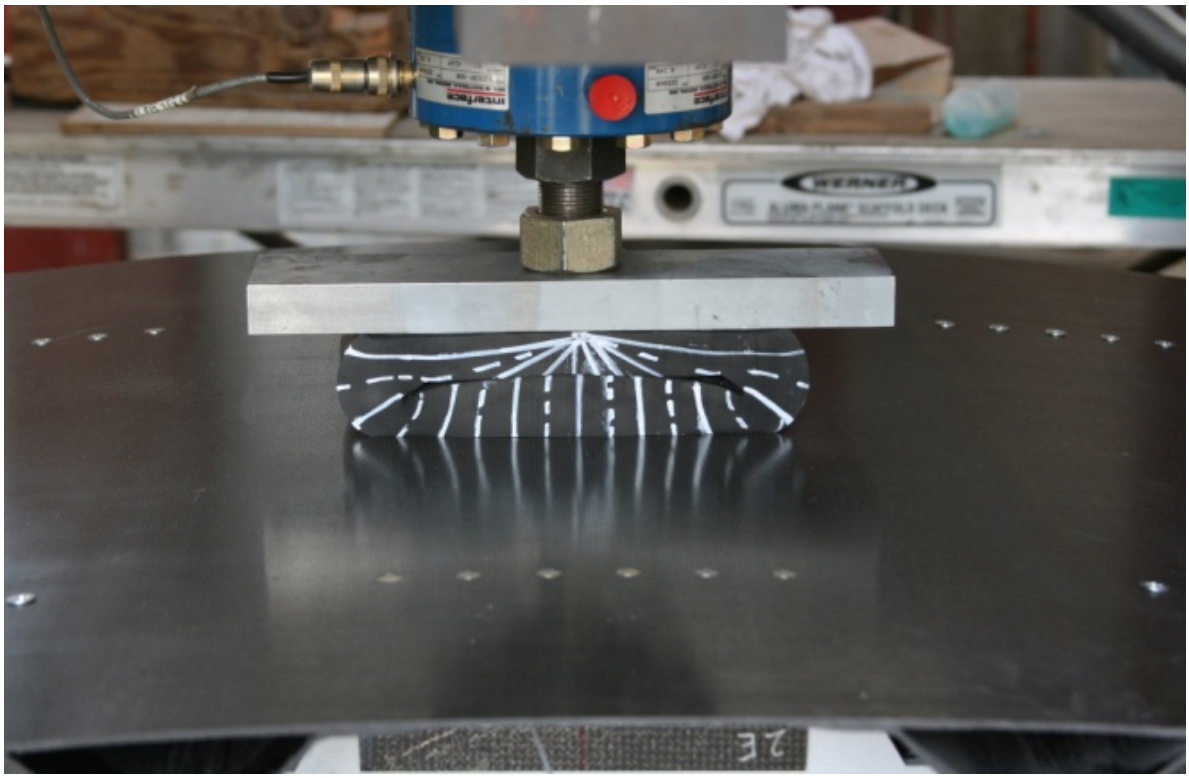

Figure 24. Contact between the rubber bumper and Stringer02 external skin

Figure 25 shows the force versus indentation curves for Stringer02. Inflections in the plots were observed at low-level loads due to the stiffening behavior of the rubber bumper as its open D-shaped cavity collapsed under compression. When the load reached approximately 2.89 kN (2–3 mm indentation), the cavity closed, and the bumper stiffened significantly.

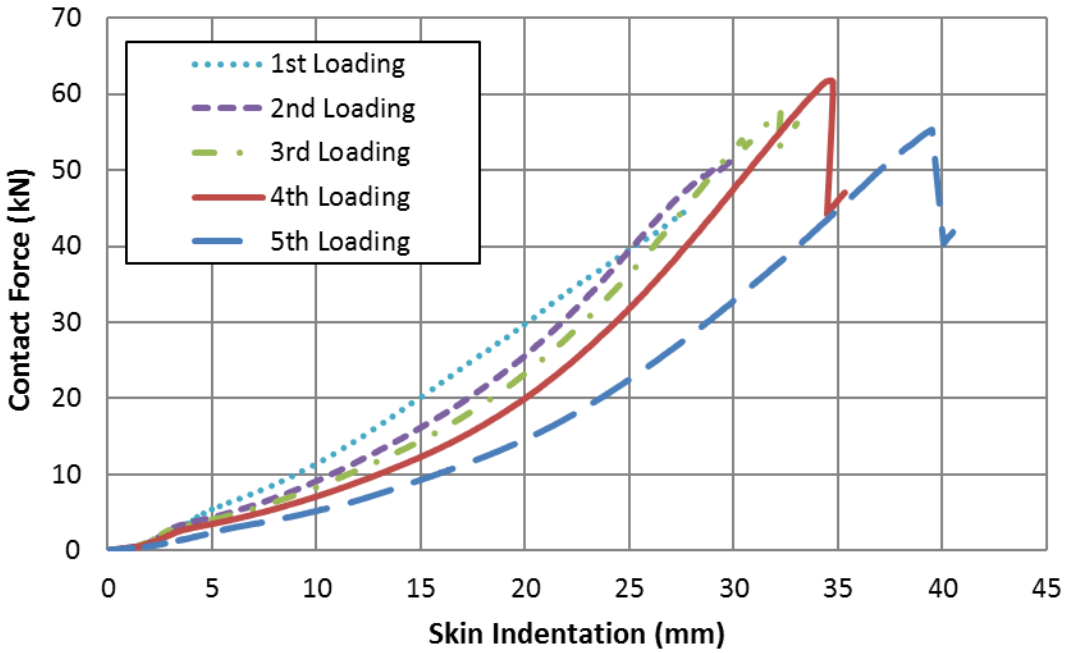

Figure 25. Stringer02 contact force vs. skin indentation plots

The first two loading cycles produced only shear-tie radius delamination failures due to shear-tie opening deformation, and some localized crushing/fiber failure at the shear-tie corners. During the first loading, clicking noises were heard at approximately 35 kN, signaling potential delamination failures in the shear ties. A loud cracking noise was heard when the panel held a load of 44.84 kN at an indentation level of 27.7 mm. When the panel was unloaded, the shear ties showed residual bending strains and visible crushing damage at the curved corners. During the second loading, active clicking sounds were again observed past 44.48 kN. Large panel deformation led to further opening of the shear ties and caused radius delamination at these locations. These shear-tie failure modes did not cause load distinct drops, but they contributed to stiffness losses.

Major failures occurred from the third load cycle onwards in the form of stringer-to-skin delamination. In addition, continued shear-tie delamination and crushing damage also occurred throughout these load cycles. During the third loading, a load drop occurred at 57.96 kN and an indentation of 32.3 mm. The load drop coincided with the two stringers delaminating from the skin, initiating at the shear-tie support locations away from the loaded area. Figure 26 shows the area of stringer-to-skin delamination damage accumulation through the fourth loading. The initial delamination locations, detected after the third load, were at the shear-tie support locations (see figure 26). During the fourth loading, a major load drop occurred at 61.33 kN contact force and 34.5 mm indentation because of the large-sized delamination growth. An interior view of the panel with the stringer-to-skin delamination is shown in figure 27. However, no visible damage was found on the skin's external surface after the panel was unloaded, despite the significant stringer-skin delamination damage and the additional fiber-crushing damage occurring in the shear ties (see figure 28). Crushing damage occurred at the edge of the shear tie contacting the stringer flange, which was in the primary load path. At the end of the fourth load cycle, the panel could still sustain a load of 47.06 kN.

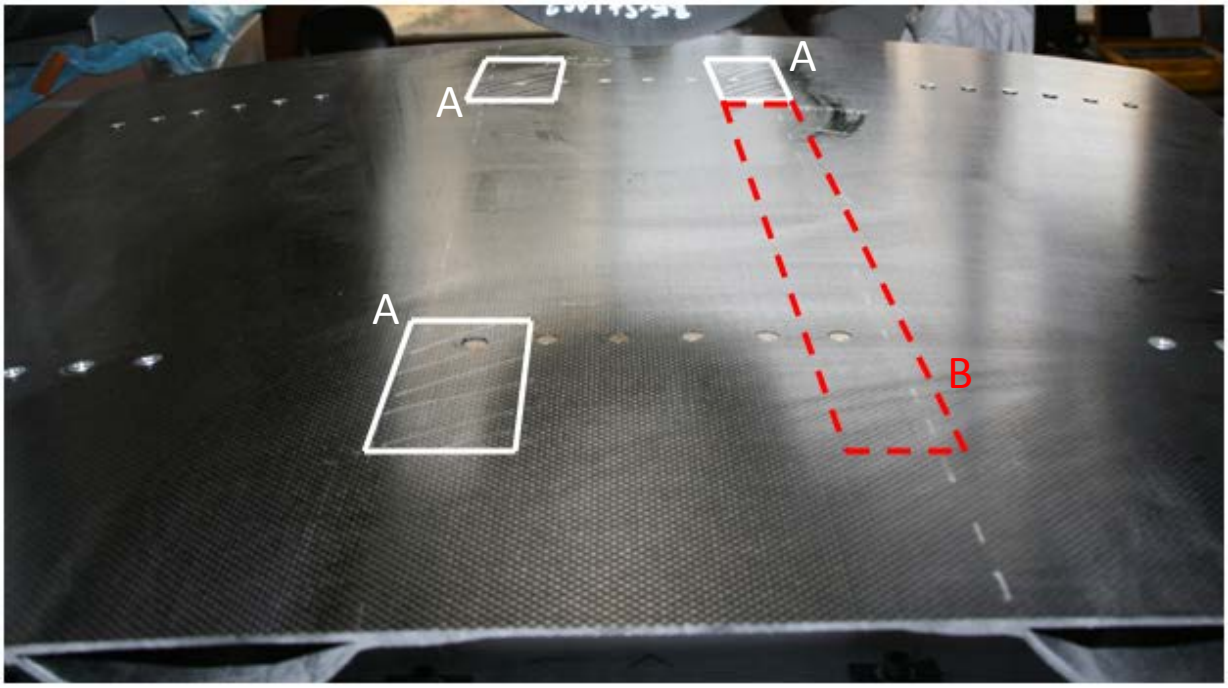

Figure 26. Stringer02 after fourth loading. The "A" boxes indicate area of delamination damage incurred during 3rd loading; the dashed "B" box indicates area of delamination incurred during 4th loading

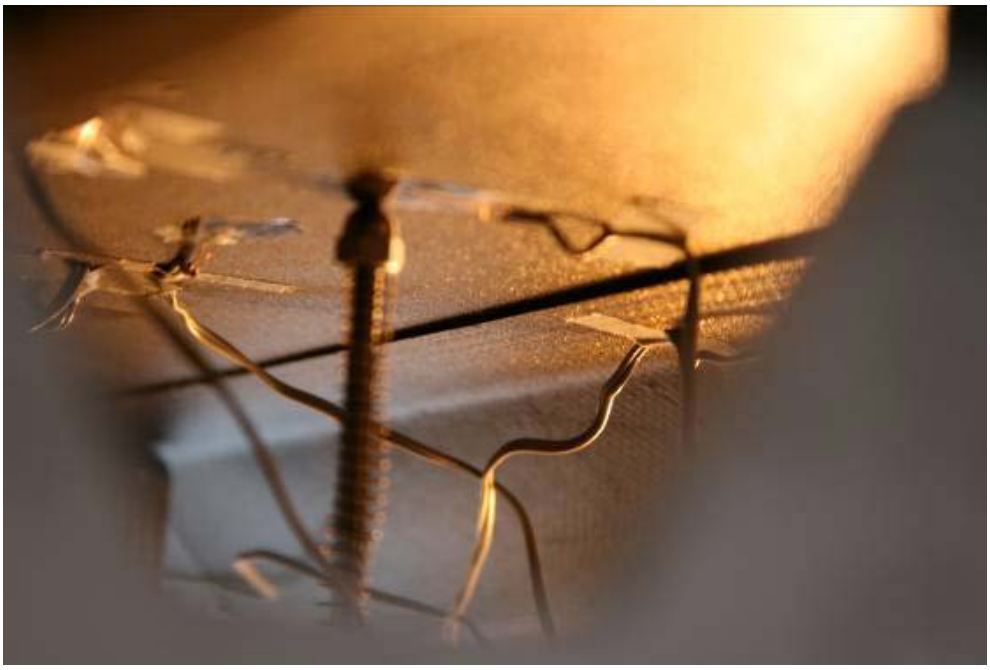

Figure 27. Interior view of the Stringer02 stringer-to-skin delamination following 4th loading

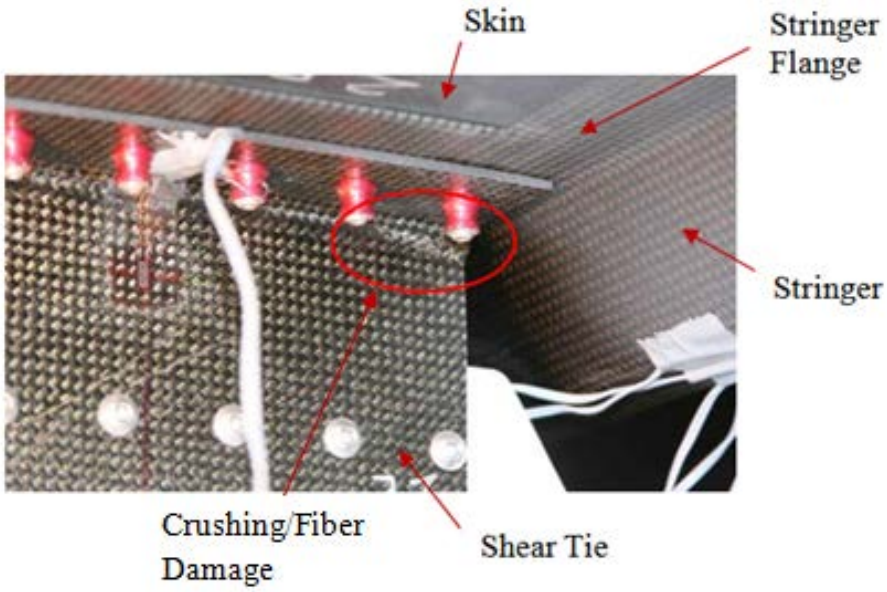

Figure 28. Stringer02 cumulative crushing damage on one of the shear ties after the fourth loading; the damage is circled in red

During the fifth load cycle, large asymmetrical panel deformation was observed because the delaminated stringer softened one side of the panel (see figure 29), and the load path was redirected toward the stringer that remained intact. The panel held a load of 55.34 kN before extensive skin-stringer delamination occurred on the second stringer as well. The delamination of the second stringer extended to the free edge of the panel. The final damage state of the panel before unloading is shown in figure 29. It was likely that the final delamination damage grew from the existing delaminations (from first to fourth loading) and extended out to the free edge rather than originating at the panel free edge and moving in.

Stiffness loss was observed for each of the load cycles (see figure 25). This was due to the cumulative damage sustained at the shear-ties corners, and the delamination growth of the stringer flanges during the fourth and fifth load cycles. Sudden damaging events, such as delamination growth, resulted in load drops. Slow damage growths resulted in gradual change in the slope of the loading curves toward the end of each load cycle. The load level at which gradual damage growth occurred was inferred by the softening seen at approximately 56 kN in the fourth loading cycle and at 51 kN in the fifth loading cycle (see figure 25). These damaging events were accompanied by audible cues of composite failure.

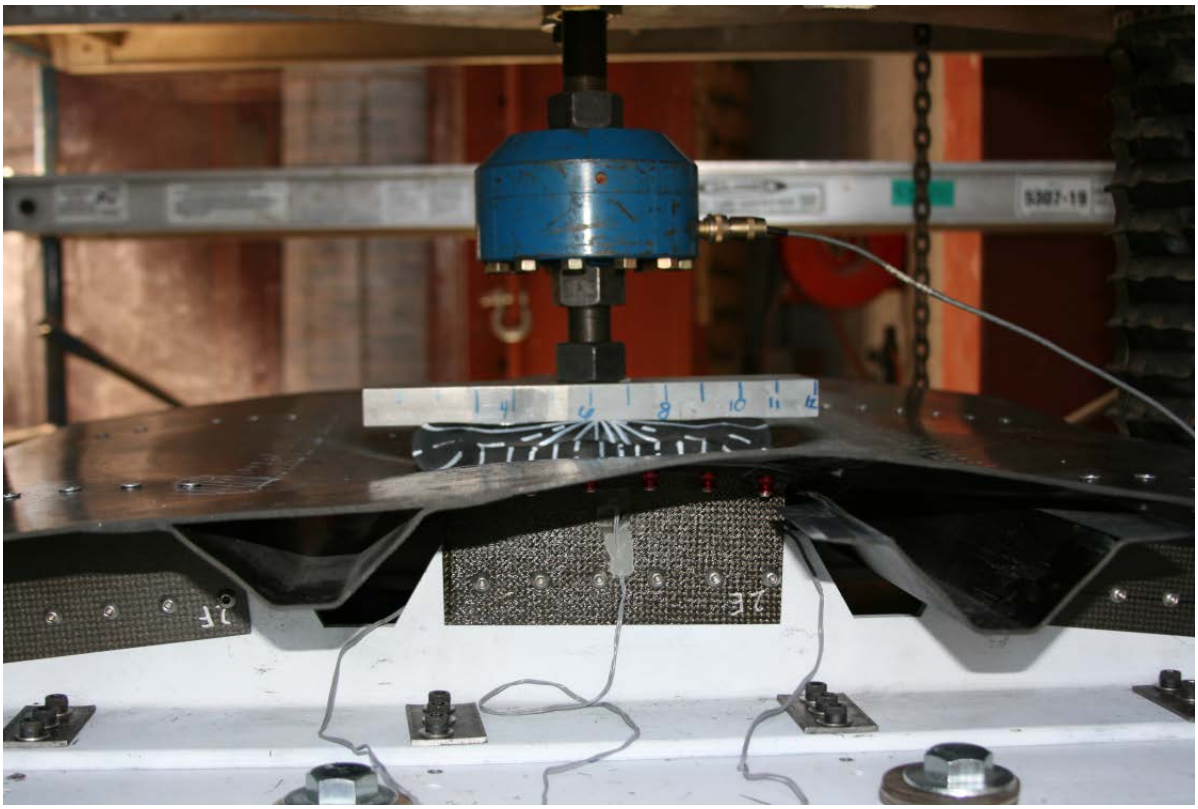

Figure 29. Stringer02 following the 5th loading; delamination of the right-side Stringer out to the free edge is observed

4.1.3 Stringer05 Experimental Results

Stringer05 was dynamically impacted at 0.5 m/sec with the TUG D-shaped rubber bumper on the panel's skin between the stringers. Only one load cycle was conducted on Stringer05. The dynamically loaded Stringer05 load versus indentation plot is shown in figure 30 along with a combined loading plot for the quasi-statically tested Stringer02. The two panels show similar stiffness response and peak loads. However, their initial failure modes and path of failure propagation were different.

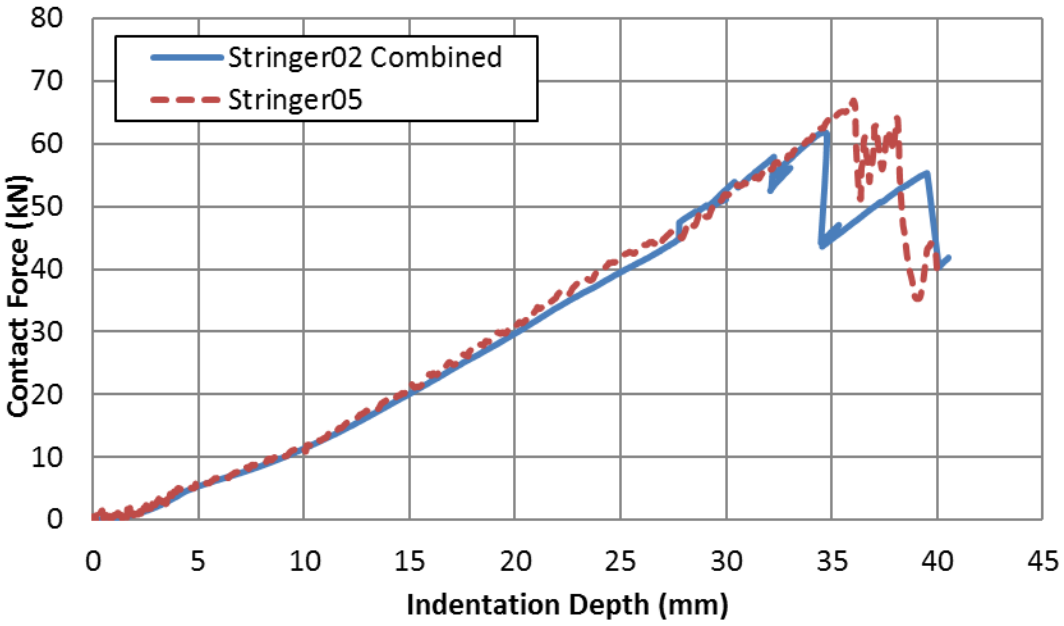

Figure 30. Stringer02 and Stringer05 contact force vs. skin indentation plots

A high-speed camera was used to provide an interior view of the panel because it was impacted from the skin exterior. The camera captured a view of the panel at the impact zone, specifically focusing on a stringer-skin connection. Figure 31 shows a series of high-speed video still-captures of the damaging events, with each event's corresponding time stamp noted. Figure 31(a) shows the stringer-skin connection at 17.2 msec after impact as an initial reference point. At this time, the panel deformation was minimal, and no damage incurred. The panel interior was partially painted white to accentuate damage. The metal rod in this figure was connected to a displacement potentiometer to track the skin deflection during impact. The green arrow in figure 31(a) points to the edge of the stringer-to-skin bond, whereas the red arrow points to the curved connection between the stringer flange and its diagonal wall (stringer heel). Both locations would experience failure during impact.

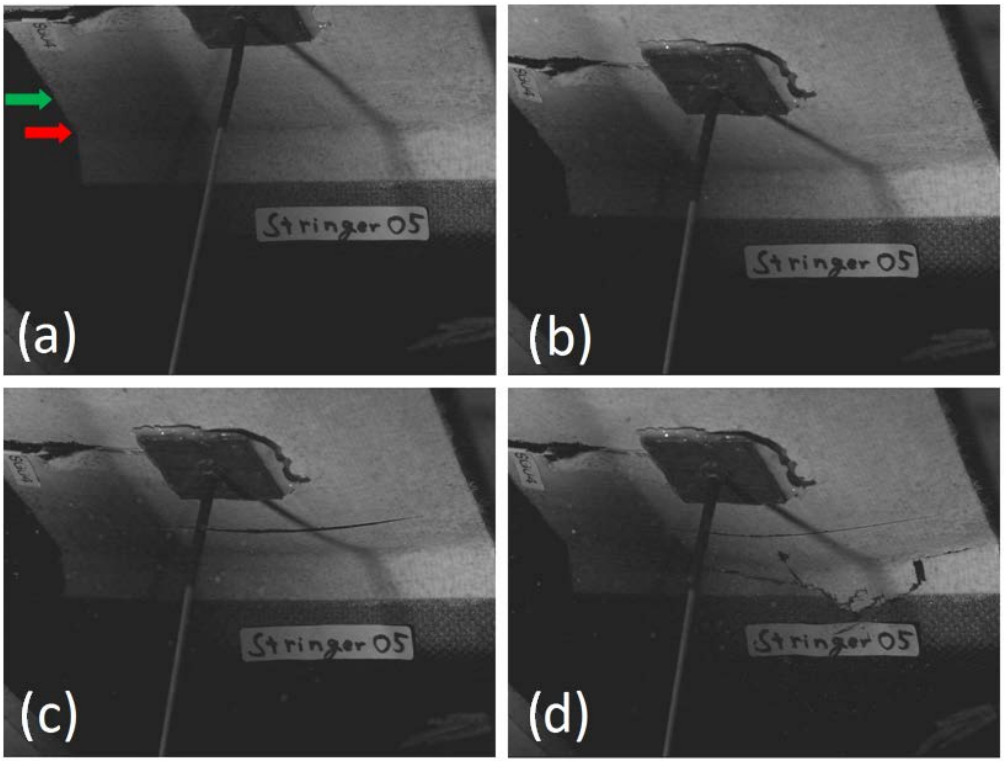

Figure 31. High-speed video still frames of Stringer05 test as viewed from the panel's interior: (a) t = 17.2 msec, (b) t = 199.0 msec, (c) t = 199.6 msec, and (d) t = 202.4 msec after impact

Two significant load-drops were observed at 36.1 and 38.1 mm of skin indentation, each corresponding to failures occurring at the stringer local to the impact zone. The first load drop at 36.1 mm of indentation was caused by skin-to-stringer delamination and stringer fracture failures on first stringer. Although its failures were not captured within the view of the high-speed camera, carbon fiber debris was seen ejected from that stringer location. Figure 31(b) shows the white carbon fiber debris falling from the out-of-view stringer at 199.0 msec after impact. The timing of this event coincided with the first load drop. This first skin-to-stringer delamination and stringer fracture failures were confirmed after the experiment. The second load drop, at
38.1 mm of indentation, was caused by similar failures at the second stringer in the impact zone. This time, the sequence of damaging events was captured by the high-speed camera. Figure 31(c) shows that the skin-to-stringer delamination initiated underneath the impactor 199.6 msec after the impact and grew toward the boundary shear ties that were outside of the impact zone toward the boundary conditions. Figure 31(d) shows stringer wall fracture failure occurred at 202.4 msec after impact, immediately following the delamination damage.

Post-test examination of the panel revealed that a through-thickness skin crack was formed along the skin-stringer joint underneath the impactor. The exact timing of the skin crack damage was not known. However, it was assumed that the skin crack occurred at roughly the same timeframe as the skin-to-stringer delamination and stringer cracking because of high shear-stress buildup. Figure 32 shows the panel surface with the through thickness skin crack. Despite the level of damage,

there was almost no global residual deformation of the skin. The only external sign of impact damage was the formation of a skin crack.

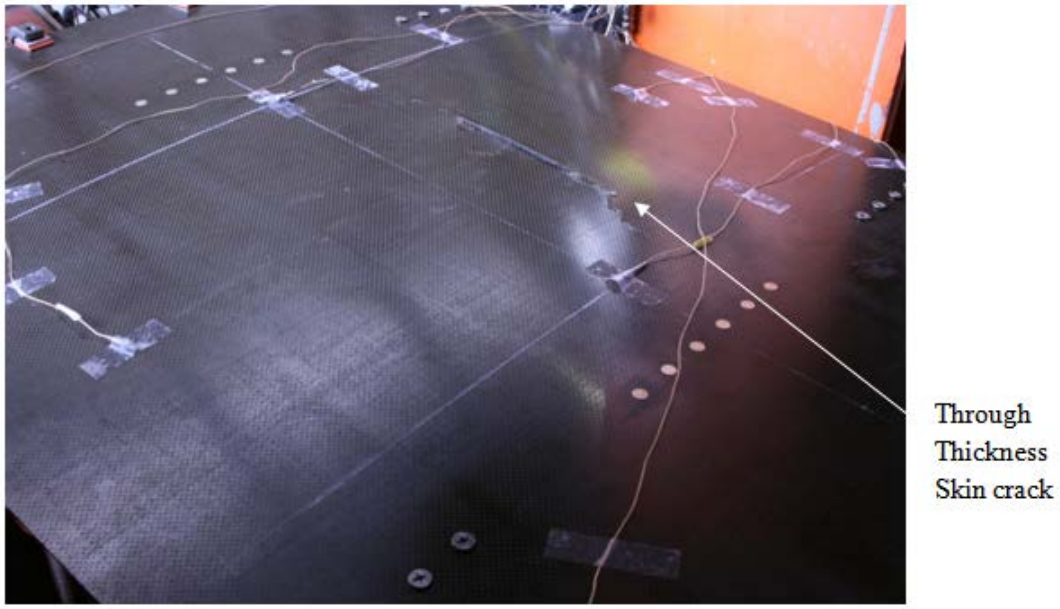

Figure 32. Post-test state of Stringer05 showing surface cracks along the skin-stringer connection at the impact location

Figure 33 shows the post-test damage from both the exterior and interior views of the panel. The skin-to-stringer delamination area is indicated by white hatch marks on the exterior view. It is important to note that all failure modes were created along the skin-stringer connections in the primary load path. Similar to the Stringer02 panel, permanent softening of the shear ties due to radial delamination and corner crushing was also found.

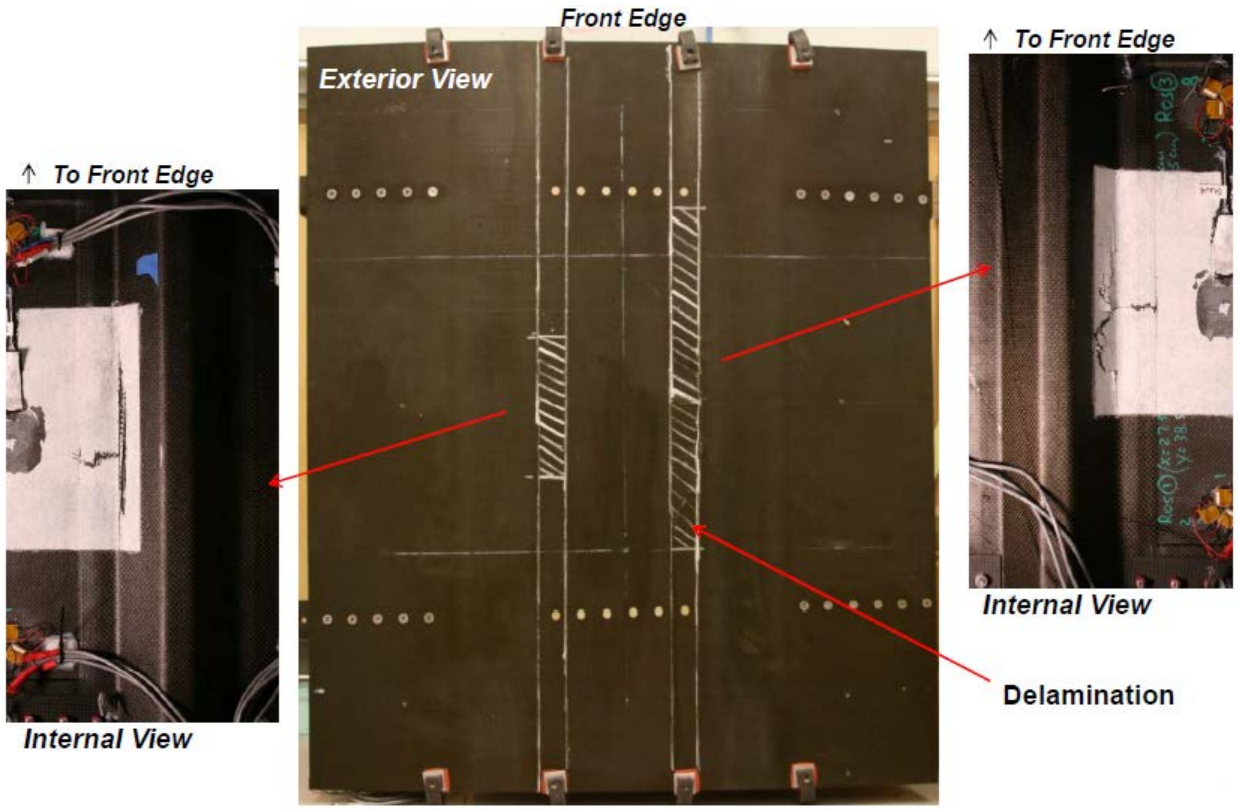

(a) (b) (c)

Figure 33. (a & c) crack formations along the stringer radii and on the flanges viewed from the interior side, and (b) post-test A-scan map of Stringer05 (hatched areas are locations of skin-to-stringer delamination);

4.1.4 Stringer00, 03, and 06 Experimental Results

The specimens Stringer00, 03, and 06 were three-stringer specimens with loading applied directly onto the middle stringer. The Stringer00, 03, and 06 panels were quasi-statically indented with an aluminum indenter, quasi-statically indented with a rubber bumper, and dynamically impacted with a rubber bumper, respectively. All three panels exhibited varying degrees of local skin cracking (see figure 34). First, the aluminum indenter used in the
Sringer00 quasi-static test produced penetration damage. Second, the rubber bumper used in the String03 quasi-static test produced light surface cracks that could only be detected with a glancing light source. Third, the rubber bumper used in the Stringer06 dynamic test produced through-thickness skin cracks.

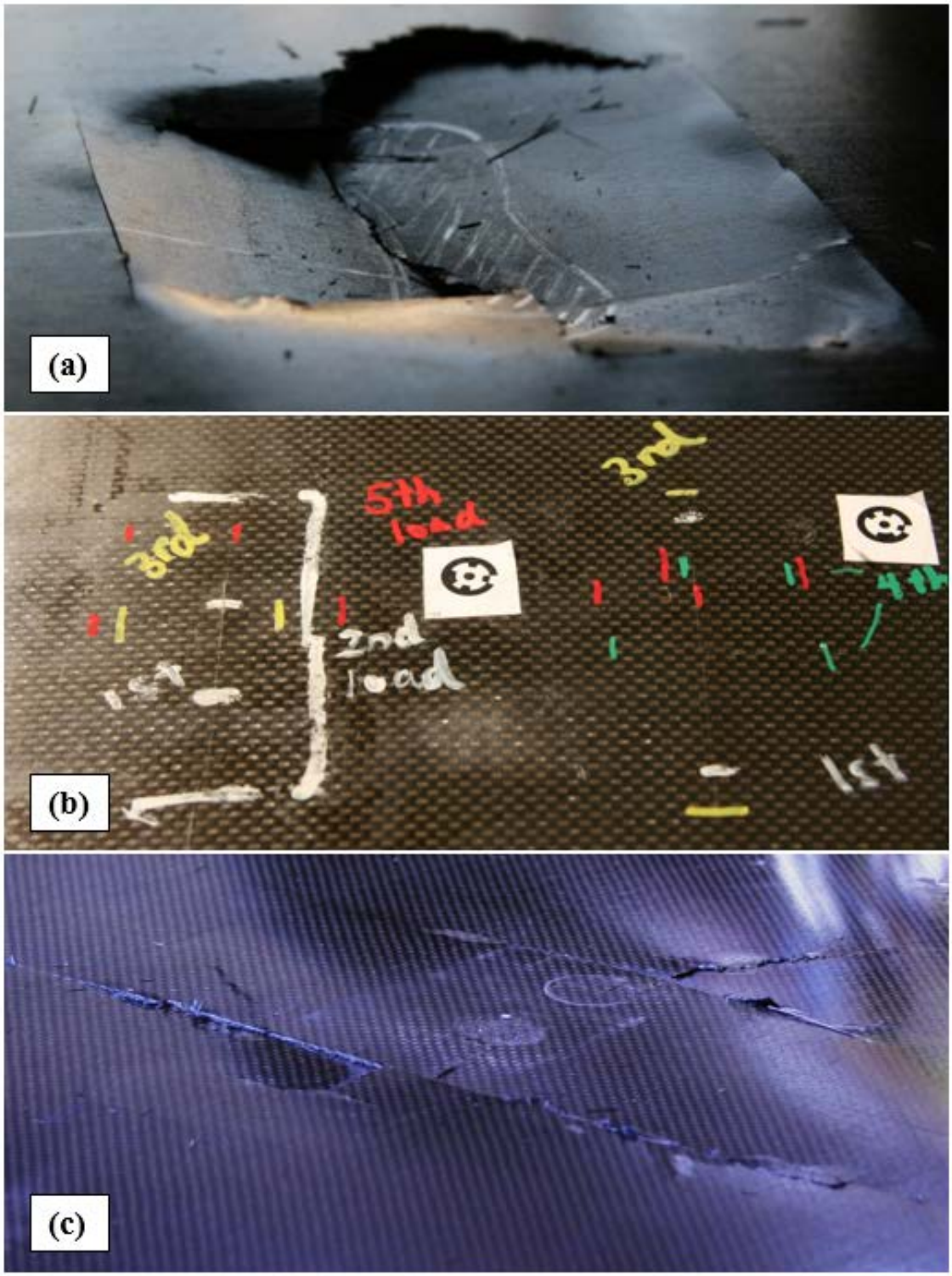

Figure 34. Final external damage states for (a) Stringer00, (b) Stringer03, and (c) Stringer06

4.1.5 Effects of Impact Location

The stringer-reinforced areas of the skin were locally stiffened, so higher forces were generated when loading was applied directly over a stringer, in comparison to loading on the skin bay between the stringers. This was evident from the comparison of the Stringer00 and Stringer01 final loading plots (see figure 35). Both were quasi-statically indented with the aluminum indenter and exhibited similar skin delamination and penetration damage, as shown in figures 23 and 34(a). Stringer00 showed a higher initial stiffness before local skin delamination was formed.

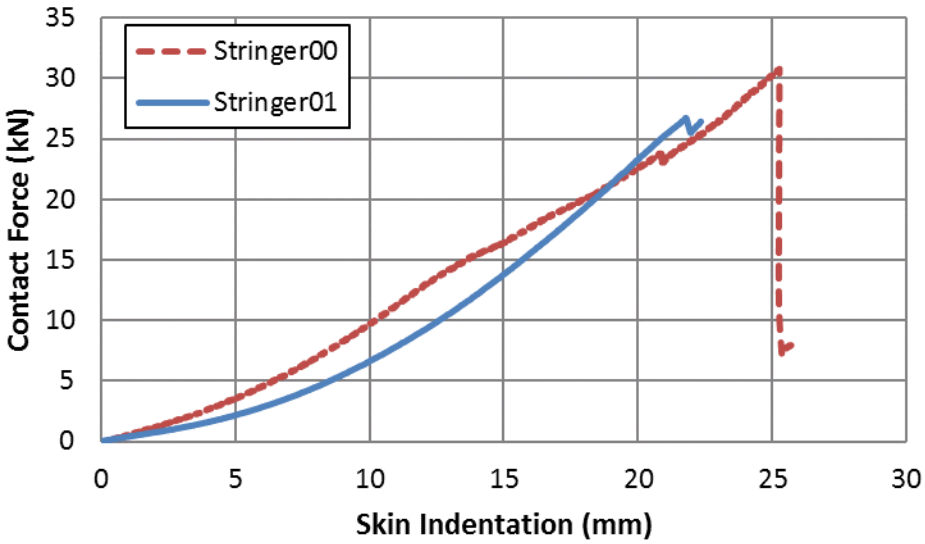

Figure 35. Stringer00 and 01 final loading contact force vs. skin-indentation plots

In addition, changing the impact location influenced the damage location. Figure 36 shows the two-stringer and three-stringer panel configurations and their primary load paths. Because the loading was applied between the shear ties (which affix to boundary conditions), loading was transferred through the stringers into the shear ties. These load paths represented the locations where damage was most likely to develop. Figure 37 shows the final delamination damage of the Stringer02 and Stringer03 panels. In the Stringer02 case (loaded on the panel skin), the load was transferred to the two adjacent stringers. Because the load was carried by both stringers, it was evenly distributed in the panel. Therefore, the delamination damage was more widespread. In the Stringer03 (loaded on stringer) case, the transverse load was carried primarily by the middle stringer because it was a direct load path to the shear-ties boundary conditions. Therefore, the delamination damage was confined to the loaded stringer. In addition, the impact location had an important effect on damage mode. The skin and stringer joints were locations of severe stiffness change and stress concentration. As shown in figure 38, transverse loading applied over the stringer induced high local bending and transverse shear stresses at the skin-stringer joining points. Therefore, loading on the stringer-reinforcement location always produced some degree of fiber cracks along the skin-stringer joints, regardless of impactor type and speed. In contrast, loading on the unreinforced skin bay location produced fewer skin cracks.

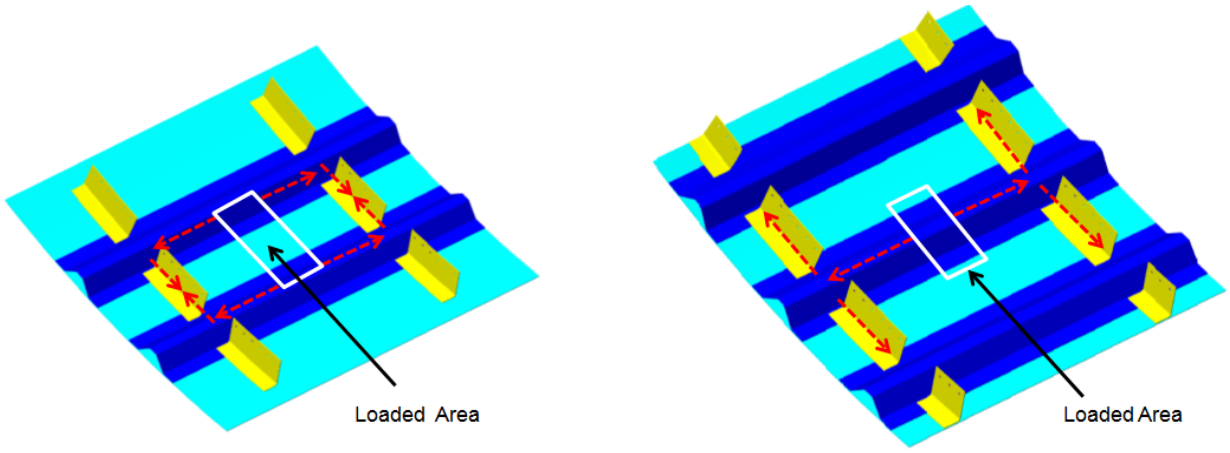

(a) (b)

Figure 36. Primary load paths of the (a) two-stringer and (b) three-stringer specimen configurations based on the location of loading

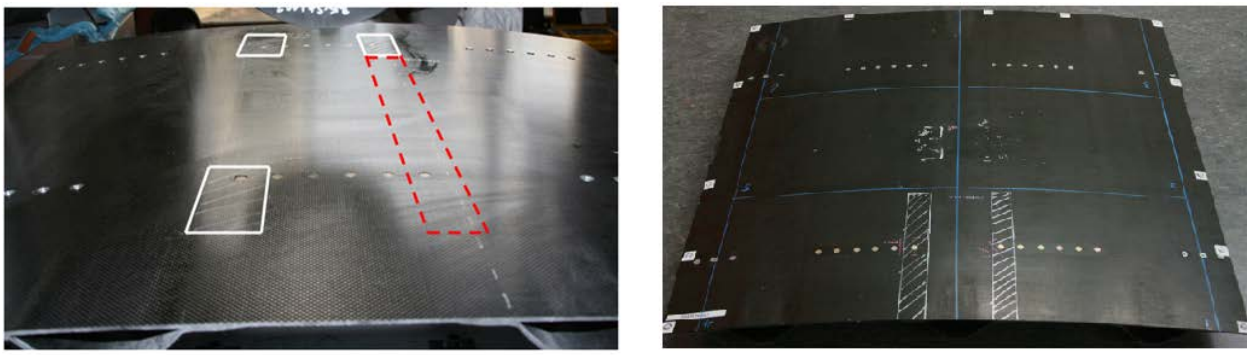

(a) (b)

Figure 37. Final delamination area of (a) Stringer02 and (b) Stringer03

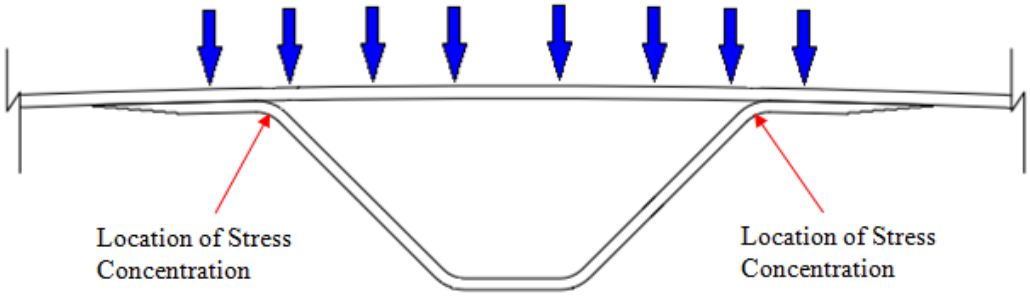

Figure 38. Cross-section view of the stringer-reinforced skin loaded over the stringer; concentrated stress is expected to develop at the skin-stringer joint

4.1.6 Effect of Impactor Type

The aluminum impactor was used in both the Stringer00 and Stringer01 quasi-static indentation experiments. Both specimens showed similar damage modes and maximum loads before failure. Because of the stiffness differences between the skin and aluminum impactor, the panel skin locally deformed around the aluminum impactor upon contact. Per the Hertzian Contact law, the contact stresses are inversely proportional to the contact radius. Therefore, the skin delamination initiated at the tighter-radius edges of the indenter (see arrows in figure 20), where the contact interaction induced the highest transverse interlaminar shear stresses. The delaminations were initially formed as two oval-shaped patches. With increasing loads, the delaminations grew and connected into an overall peanut-shaped zone (see hatched zones in figures 23 and 34(a)). Following the delamination damage, increasing contact load eventually led to local skin perforations.

Alternatively, the rubber bumper loading produced widespread damage because of the larger contact area, resulting in lower local stresses and an overall higher level of loading being applied. During the rubber bumper loaded experiments, the bumper deformed hyperelastically as it flattened before the buildup of higher contact forces. The bumper contact area increased to approximately 8400 mm^2. Therefore, the contact pressure and the resulting interlaminar stresses were lower relative to the metal indenter, particularly at the softer surrounding boundary of the bumper. When the bumper was fully flattened, transverse loading was applied over the stringer-skin connections (i.e., stringer flanges) because of the larger contact length, allowing a direct load path into the stringers (see figure 39).

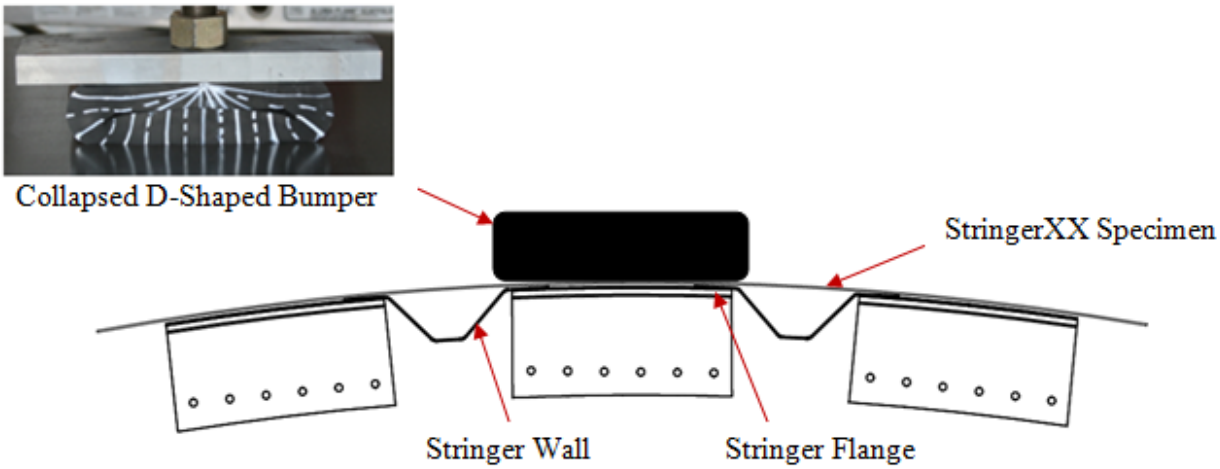

Figure 39. Photo and illustration of D-shaped bumper collapsed during load

The Stringer02 (loaded on skin mid-bay) and Stringer03 (loaded on stringer) specimens were both quasi-statically indented with the rubber bumper. Unlike what occurred in the rigid aluminum indentor experiments, Stringer02 and Stringer03 did not experience local delamination directly under the indentor. The local contact stresses were reduced, leading to higher contact load buildup before failure and widespread stringer-to-skin delamination. The Stringer02 specimen sustained stringer-to-skin delamination along two stringer flanges adjacent to the bumper loaded area (see figure 37). The stringer-to-skin delamination damage initiated at a location away from the impact

zone, at the boundary support locations. With increasing contact load, the stringer-to-skin delamination grew inward, toward the middle of the panel. Likewise, the Stringer03 specimen initially developed stringer-to-skin delamination away from the impact zone at the edge of the panel. However, additional local skin-crack damage was also found in Stringer03 because of its impact location over the stringer-reinforced skin.

4.1.7 Effect of Loading Speed

The effect of the loading speed was observed by comparing the Stringer02 with the Stringer05 results. As the hollow D-shaped bumper was compressed and flattened, the bumper contact area increased, allowing the load to transfer directly into the stringers. Therefore, damage was found primarily along this load path. Figure 40 shows the load path through these stringers can be idealized as a beam-bending response, which includes the shear-force diagram along the stringers.

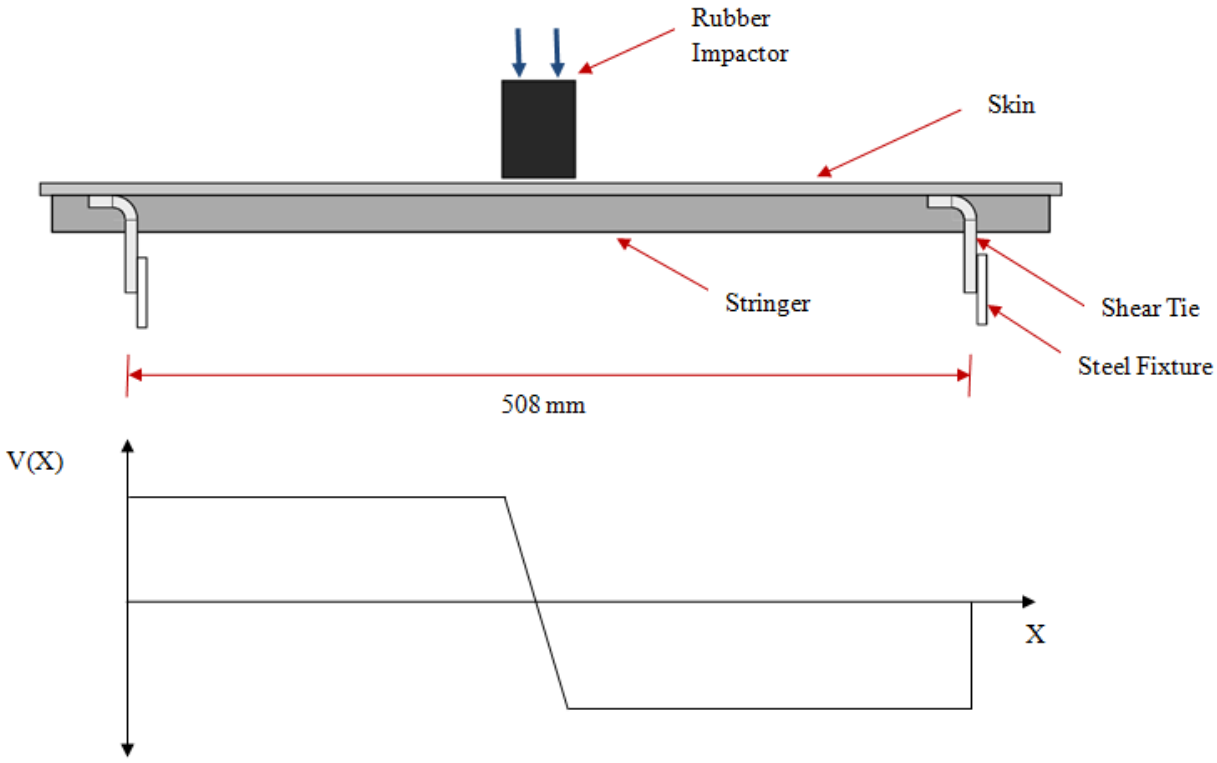

Figure 40. Side view of the panel: the impact experiments can be idealized as beam bending of the stringers; the shear force diagram of stringer is also shown

The stringers were 508-mm-long beams supported at the ends by the shear ties. A distributed pressure load applied over a section at the midspan of the beam by the bumper produced transverse shear stresses, which could develop higher localized values at the impact zone and at the geometrical transitions between the stringer and shear ties. These locations were the most susceptible to delamination failure. Therefore, skin-to-stringer delamination and fracture failures initiated at these locations. Dynamic localization of the panel response can be used to explain the differences between the two test results. In the Stringer02 (quasi-static) test, skin-stringer separation initiated at the shear-tie support locations, whereas in the Stringer05 (dynamic) test, the

same damage initiated locally under the impactor. The Stringer05 panel also sustained additional stringer and skin cracks at the impact zone. These damage modes indicate that dynamic localization can influence the panel deformation shape and stresses, even at a low-impact speed of 0.5 m/sec, because of the large specimen size.

Figure 41 shows the time-dependent deformation response of a beam undergoing dynamic three-point bending at various times after the impact. The first three diagrams in figure 41 show the initial deformation responses of a beam immediately after dynamic impact. These deformation modes are influenced by inertial effects and higher-order mode shapes, for which the central portion of the panel is mainly reacting against the dynamic load. The boundary reactions do not balance with the loading, and localization of the loading does not allow equal shear-force distribution across the beam length. Therefore, higher stresses exist at the center of the beam. As the time after initial contact increases or as the loading speed decreases, deformation of the beam transitions into a quasi-static response similar to Stringer02, as shown in the last sketch in figure 41. In this case, the applied load is balanced by the reaction forces at the outer boundaries. Because transverse shear stresses at the indented zone were reduced by the soft rubber contact, skin-stringer delamination did not initiate at the indentation zone in Stringer02; rather the damage started at the locations of the outer boundaries where contact with the stiff shear tie induced higher shear stresses.

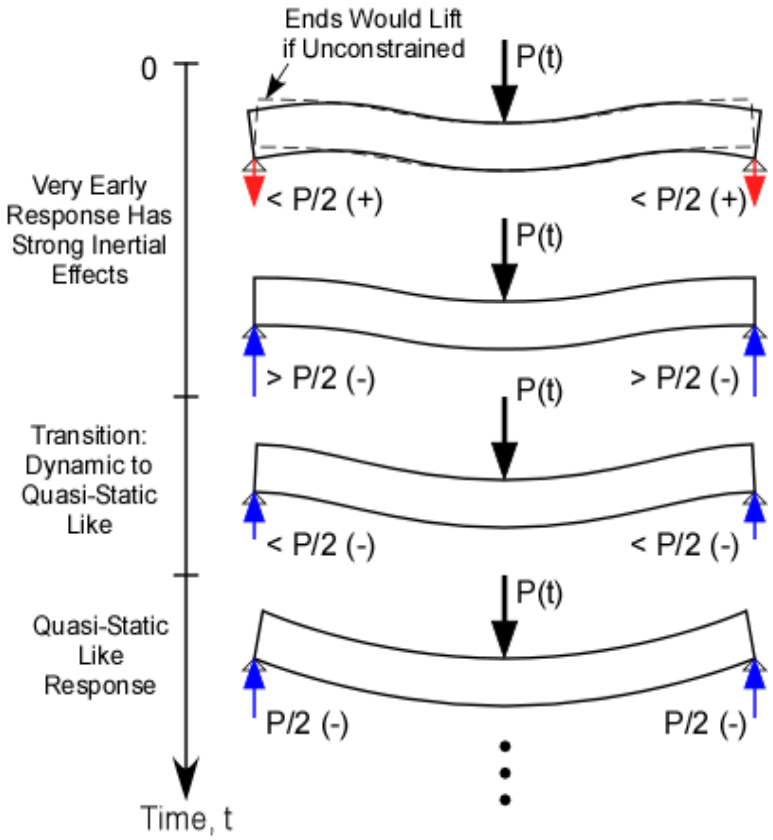

Figure 41. Time-dependent deformation response of a dynamically impacted beam

Strain gauge data also showed supporting evidence of the dynamic localization effect. Strains from both the impact zone (skin bending shown as in-plane tension) and the boundary area (shear-tie compression) are compared between the two specimens in figure 42. The overall strain pattern was similar for the two specimens. However, they showed deviation from 50–90 mm of actuator displacement, after the bumper had collapsed. The dynamic specimen experienced a higher tensile strain at the impact zone than the quasi-static specimen. Meanwhile, its compressive strain at the boundary area was lower compared to the quasi-static specimens. The observed dynamic strain deviations corresponded with the dynamic-response diagram shown conceptually in figure 42, where boundary reactions lagged behind impact-loading magnitude.

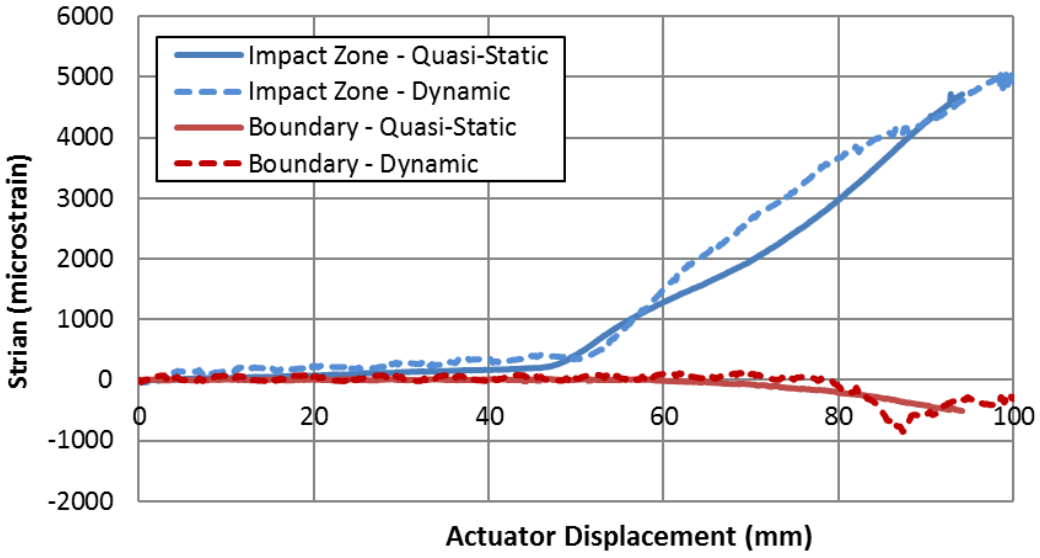

Figure 42. Strain vs. actuator displacement data taken at the impact zone (skin bending) and at the boundary area (shear-tie compression) for both the quasi-static (Stringer02) and dynamic (Stringer05) experiments; dynamic loading via 0.5 m/s constant rate actuator movement

4.2 FRAMEXX DYNAMIC EXPERIMENTS

Three-frame panels and five-frame panels were tested to explore damage modes occurring to the internal structure, particularly the frame. Because the three-frame panels (specimen IDs Frame01 and Frame02) were quasi-statically loaded, in part to prepare for the dynamic loading of the five-frame panels (specimen IDs Frame03 and Frame04), the results of these three-frame panels are not reported herein.

The five-frame panels Frame03 and Frame04 were dynamically impacted and are reported on in detail. The overall specimen layouts were identical, but they were tested under different conditions with specimen Frame03 tested at 0.5 m/s and Frame04 having two different shear-tie types—composite (Frame04-1) and aluminum (Frame04-2)—tested at 0.25 m/s (see figure 8). Figure 43 shows the layout of these specimens. The panels were 1829 mm x 2438 mm in dimension. Each panel had four stringers arranged at 305 mm apart and five C-frames arranged at 457 mm apart. The impact zone spanned across the three middle C-frames. The impact location was on the skin

spanning between stringers because this represented a more critical impact scenario where internal damage could more likely be created without visible outer skin cracking.

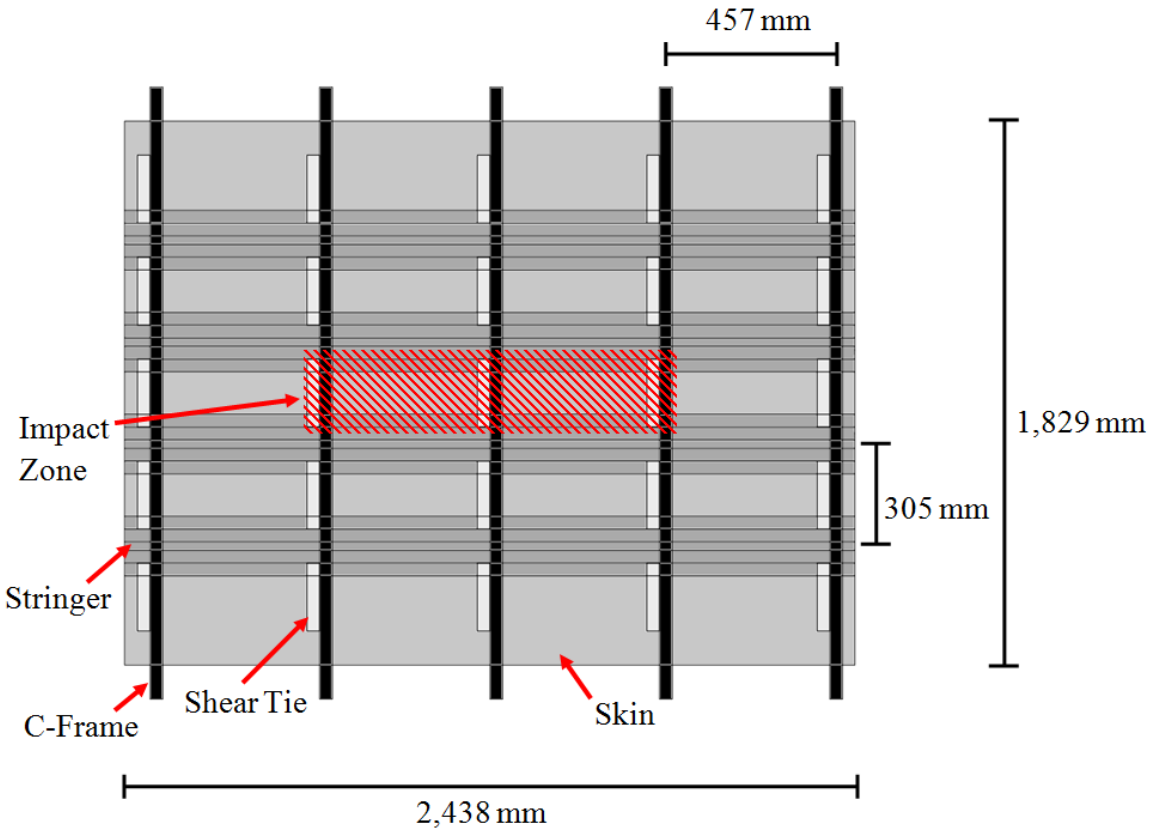

Figure 43. Plan view of specimen Frame03 and Frame04 panel configuration and loading location

Figure 44 shows the FrameXX dynamic experimental setup, including an overview drawing of the entire test setup. The specimen rested on top of two concrete blocks to allow for access underneath the panel. The C-frame was simply supported and rotational-stiffness boundary conditions. Dynamic loading was applied to the specimen by a servohydraulic actuator to which a 1.0 m long cylindrical rubber bumper (see figure 15) was mounted. The actuator was suspended vertically from a heavy steel I-beam framework.

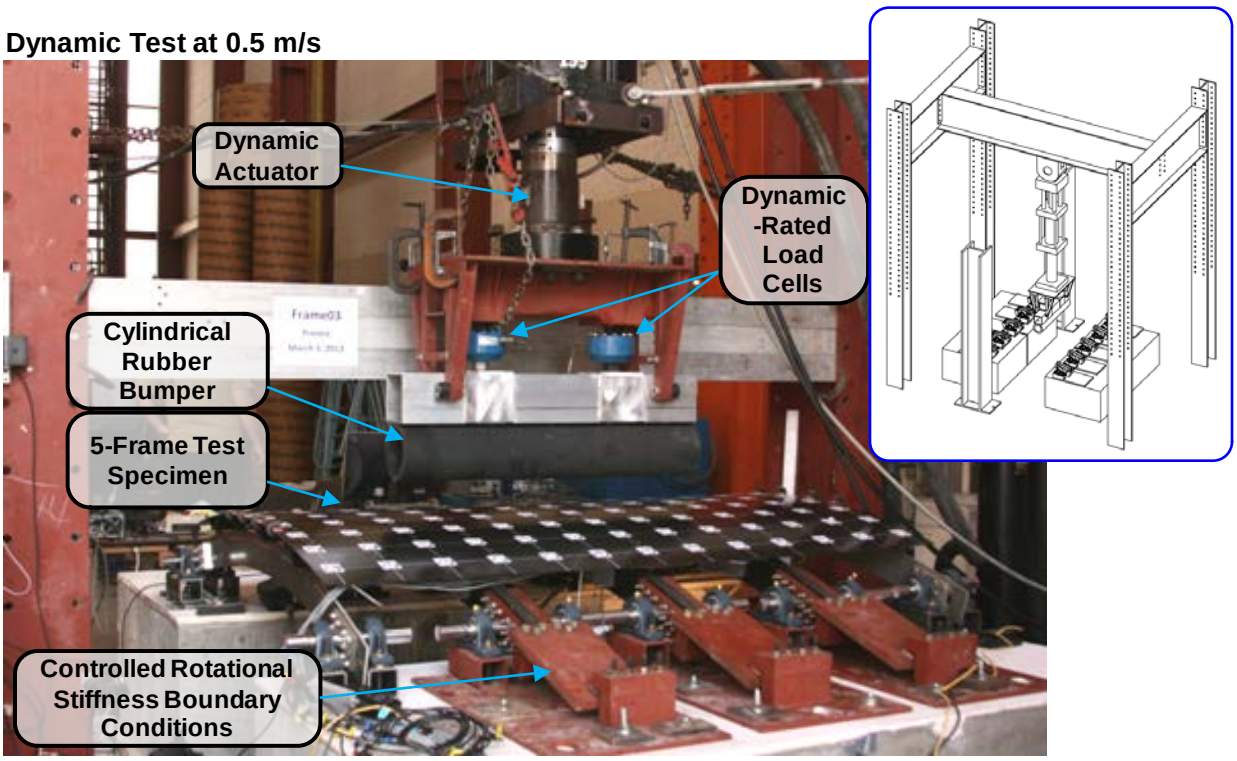

Figure 44. Experimental setup for Frame03 and 04 dynamic experiments

4.2.1 Frame03 Experimental Results

The Frame03 specimen was dynamically loaded two times with displacement-controlled actuator strokes. Each loading was applied at a constant velocity of 0.5 m/sec, followed by a 0.5 sec pause before unloading. The peak displacement values were decided based on previous quasi-static experimental results to generate similar shear-tie and C-frame damage modes.

Figure 45 shows the contact force versus skin indentation plots for both load cycles. The first loading had a total actuator displacement of 159 mm, which included an initial gap of 6.4 mm between the bumper and panel surface. The cylindrical bumper had a hollow inner diameter of 127 mm, so the resulting displacement of the specimen skin was approximately 20 mm for this loading. The initial failure mode was delamination at the curved corners of the shear ties. Moderate crushing damage of these shear-tie corners was also found (see figure 46). Note that the interior of the carbon-fiber panel was painted white to visually accentuate damage. The delamination and crushing damage occurred in all three shear ties in the impact zone shown in figure 43. They were created because of high localized bending and shear stresses induced by direct compression. These failures are indicated as event D1 in figure 45. Based on ultrasonic
A-scan inspection from the panel exterior, no delamination between the skin and stringers occurred.

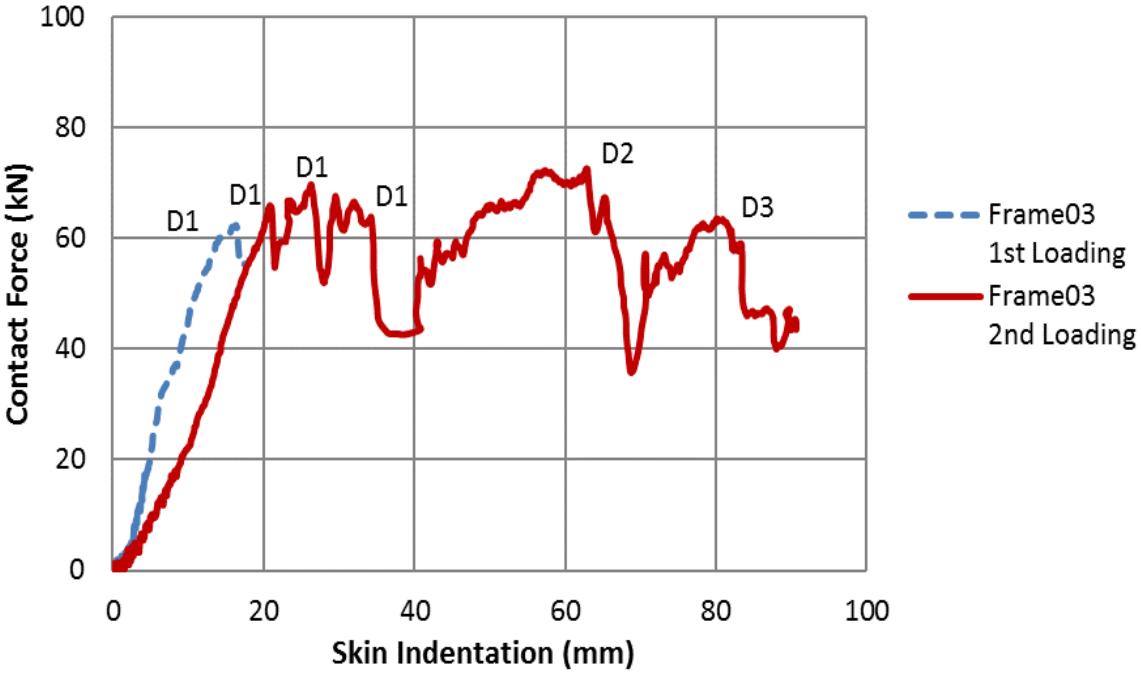

Figure 45. Frame03 contact force vs. skin indentation plots; D1 = initial three shear ties failing; D2 = additional six shear ties failing; and D3 = frame failure

Figure 46. Shear-tie corner crushing failure after first loading of panel Frame03; shear tie painted white to visually accentuate cracks

The peak actuator displacement of the second loading was 222 mm, resulting in 90 mm skin displacement (due to initial gap and hollow bumper). As shown in figure 45, the initial portion of the reloading curve was less steep compared to the first loading, intercepting the first loading curve where the first test was stopped. This suggests that the stiffness of the panel was reduced because of the pre-existing damage in the shear ties incurred during the first loading.

Figure 47 shows a series of time-lapse still images of a C-frame during the second impact loading, taken with a high-speed camera. The C-frame was viewed from the specimen's interior. The middle shear tie in the figures 47(a), (b), (c) and (d) was in the direct impact zone.
Figure 47(a) shows further crushing damage at the shear-tie corners that corresponded to events D1 in figure 45. Upon complete fracturing of the three impact-loaded shear ties, the load dropped significantly at a skin displacement of 35 mm due to the loss of load-bearing capability in the broken shear ties. Following shear-tie fracture, the gaps between the stringers and the C-frames closed as they came into direct contact, as shown in Figure 47(b). High-contact forces existed during this stringer-frame contact, which was confirmed by the scuffmarks left on the stringers by the C-frames. Therefore, the load increased between 40 and 60 mm of skin indentation (see figure 45).

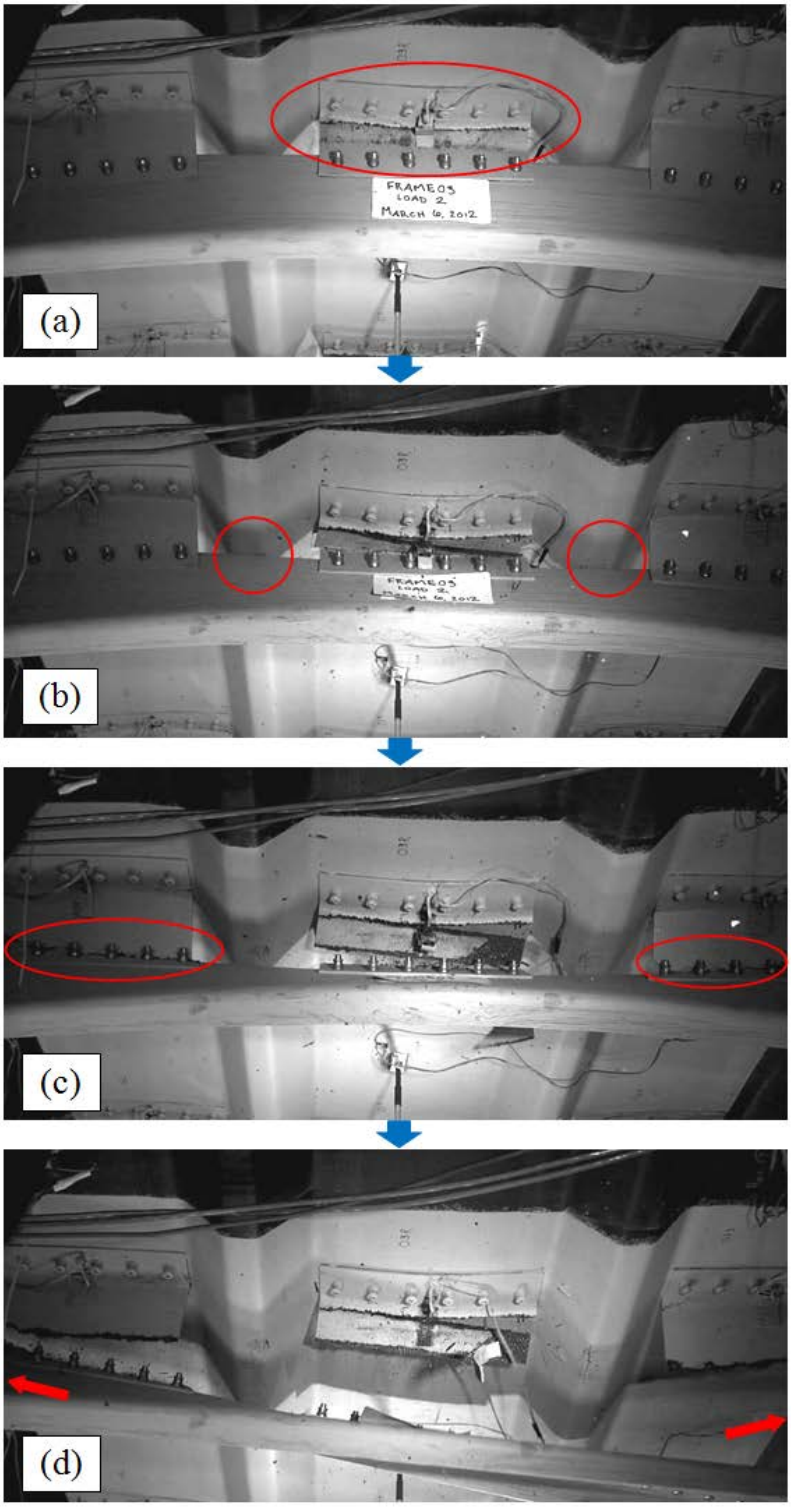

Figure 47. High-speed video stills of Frame03 2nd loading: (a) fracture of the impacted shear tie; (b) contact between the C-frame and stringers; (c) fracture of the shear ties adjacent to the impact zone; and (d) off-screen fracture of the C-frame at the boundary locations

The severed shear ties allowed for C-frame twisting during contact with the stringers, which led to widespread shear tie and C-frame failures outside the impact zone. As the impactor displacement increased, the C-frames twisted, putting moment load on the six shear ties adjacent to the impact zone. Failure of these outer shear ties occurred next, as shown in figure 47(c), and corresponded to the events indicated as D2 in figure 45. The resulting major load drop at 63 mm occurred because of the shear ties failing and subsequent unconstrained frame twisting. The final failure (D3 in figure 45) occurred at 83 mm skin displacement in the C-frames. The C-frames fractured near the boundary fixture under a combination of torsion, bending, and shear load, as shown in figure 47(d) (high twist visible, but fractures were outside of photo's field of view). Note that the series of images in figure 47 showed increasingly widespread damage as the actuator displacement and the degree of C-frame twisting increased. Although the damage initiated with the shear tie in the impact zone, C-frame rotation allowed shear-tie fractures well away from the impact zone and, eventually, C-frame fracture near the boundary conditions of the specimen.

In summary, the final internal damage state is shown in figures 48 and 49. Nine shear ties fractured—three in the impact zone (event D1 in figure 45) and six adjacent to the impact zone (event D2 in figure 45). All three impacted C-frames fractured, indicated as event D3 in figure 45. A view of the outside surface of the specimen after impact is shown in figure 50. The thin skin design was very flexible when impacted against a non-stringer reinforced location. Therefore, the skin rebounded after the experiment. No external skin-cracking damage was visible, and the permanent residual skin deformation was measured to be 4.5 mm 24 hours after the test. Skin deformation was measured by a photogrammetric technique in which the panel surface was digitally constructed based on photographs of the panel (targets seen in figure 50). The visual detectability of a 4.5 mm dent existing over a dent span of more than 1 m was difficult to perceive by visual observation.

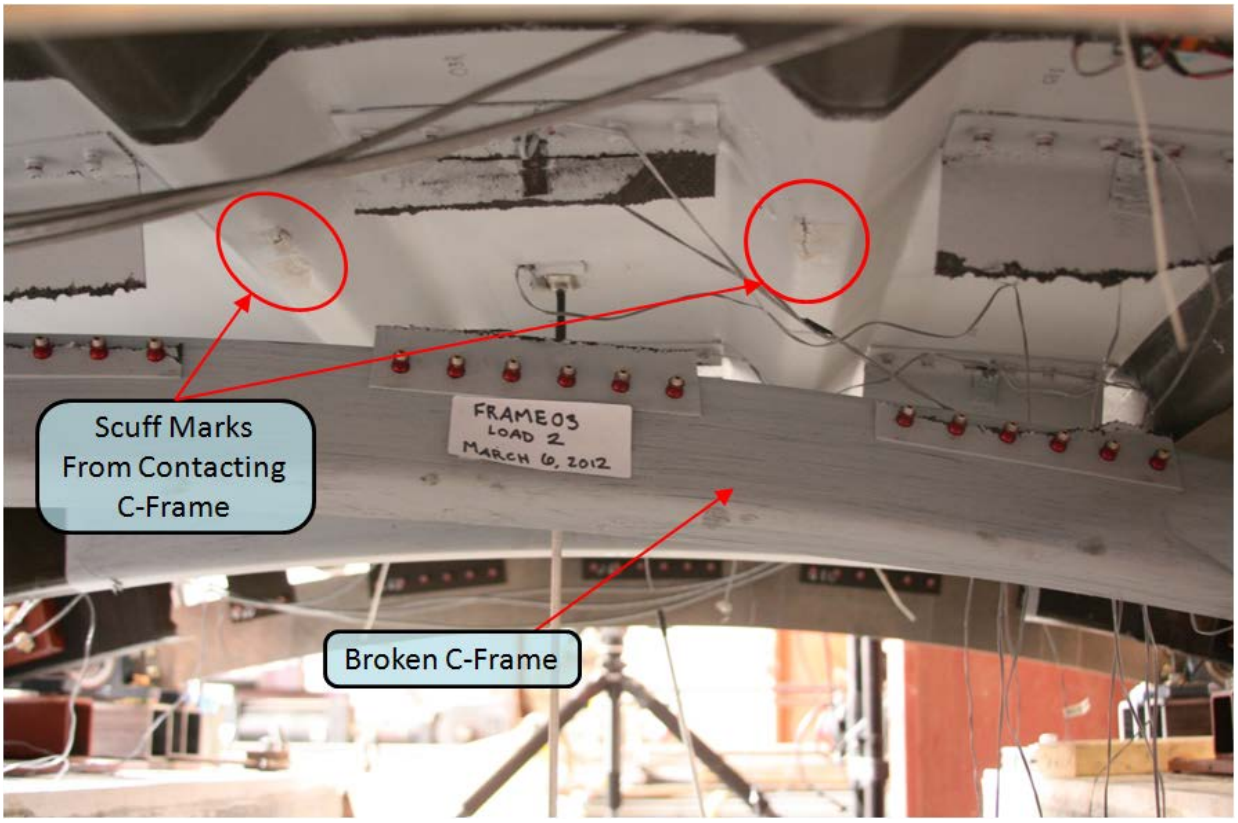

Figure 48. Frame and shear-tie damage of Frame03 after 2nd loading

Figure 49. Frame03 C-frame fracture failures near boundary supports

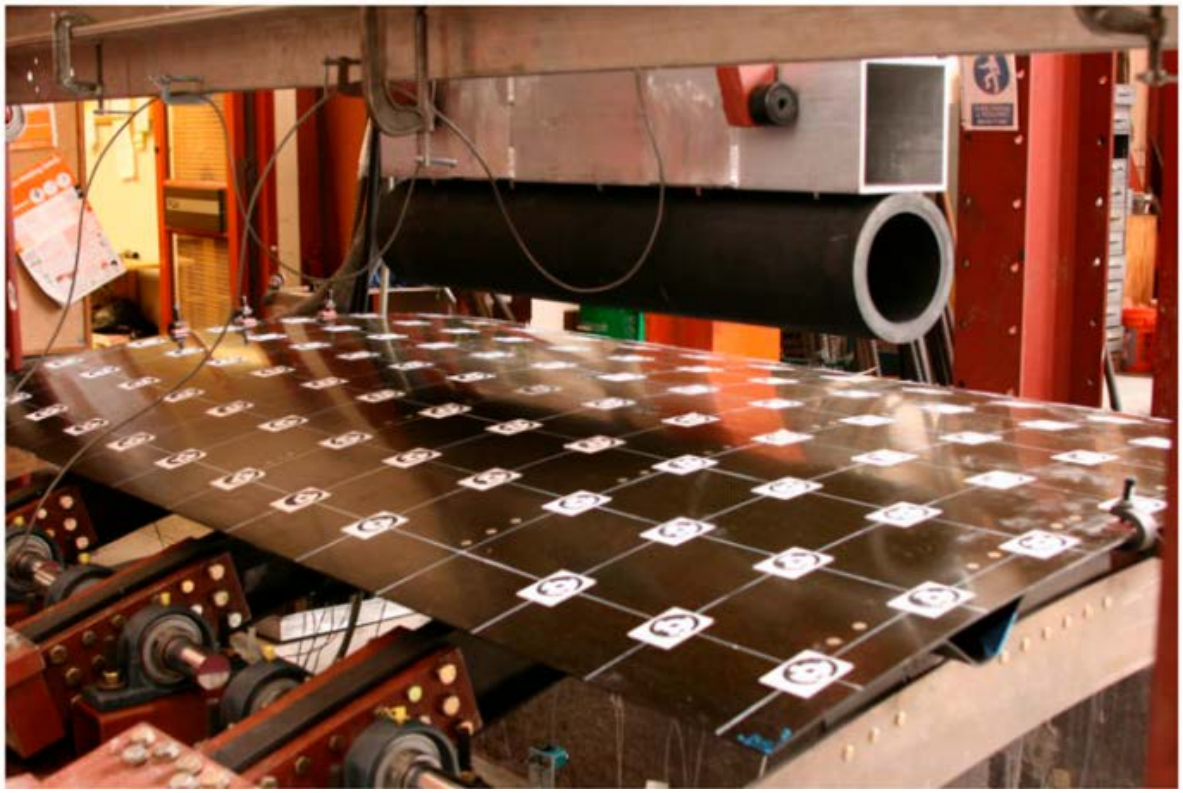

Figure 50. Frame03 external skin after loading sustaining internal C-frame damage; no externally visible damage

4.2.2 Frame04 Experiments

The second five-frame panel, Frame04, was tested in two configurations, designated as Frame04-1 and Frame04-2. Common components included the stringer-stiffened skin, frames, and shear ties located away from the impact zone. Different components included the nine shear ties within and adjacent to the impact zone.

4.2.2.1 Frame04-1

Two additional loading scenarios were explored using the Frame04 specimen. Under the assumption that Frame03's second loading data were compromised by the pre-existing shear-tie damage from the first loading, another dynamic experiment was conducted in an attempt to fill in the data gap. The load at which complete shear-tie fracture occurred was specifically questionable because of the pre-existing delamination induced during the first loading (see figure 46), likely resulting in lower peak load during the second loading. Therefore, the Frame04-1 panel specimen was designed to be identical to Frame03, but was impacted for a maximum actuator displacement of 180.3 mm to determine a pristine panel response through the point of the initial three shear ties fully failing. The Frame04-1 contact force versus skin indentation result is plotted along with the Frame03 results in figure 51 for comparison. The initial loading up until first delaminations (event D1) at 60 kN (20 mm skin indentation) was identical to specimen Frame03. Without unloading, the increasing stroke resulted in much higher load, 90.56 kN due to the continuous actuator stroke leading to complete fracture of the directly loaded three

shear ties in the impact zone. The Frame04-1 panel generated a similar level of shear-tie-crushing failures, as observed in the Frame03 panel (see figure 47(a)) at 180.3 mm displacement stroke.

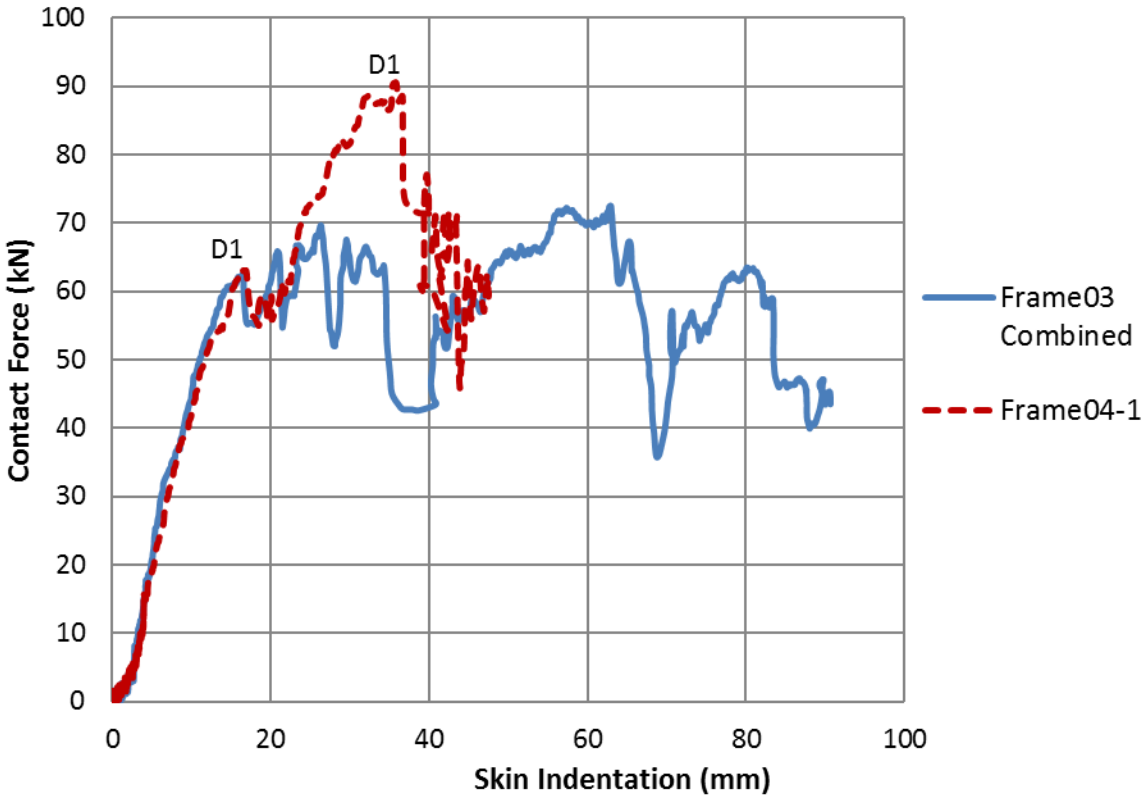

Figure 51. Frame04-1 and Frame03 contact force vs. skin indentation plots

Because the load versus displacement data of test Frame04-1 overlaps with the first loading of Frame03 and intersects with the second loading of Frame03 after the directly loaded shear ties fails, the data of Frame04-1 and the second loading of Frame03 can be combined to represent the continuous loading of a pristine panel until frame failure.

4.2.2.2 Frame04-2

With the early shear-tie delamination and fracture failures observed in the Frame03 and Frame04-1 experiments, interest existed in what was the effect of stronger shear ties on the panel response. Because the Frame04-1 test resulted in only damage to the first three shear ties directly loaded in the impact zone, with possible (not obvious) damage to the adjacent six shear ties, the central nine composite shear ties were removed and replaced with more substantial shear ties (see figure 8), and the panel was renamed as Frame04-2.

The new configuration enabled the assessment of the impact behavior of a fuselage panel with shear ties that could resist early delamination and fracture failures. Frame04-2 was otherwise identical to Frame03 in layout and loading: The new shear ties made from aluminum alloy 7075 are thicker at 3.18 mm (compared with 2.4 mm composite) and wider at 254 mm, where it mounted to the C-frame, allowing an additional two fasteners. Figure 52(a) shows the shear ties as they

were mounted to the Frame04 panel at the impact zone and adjacent to the impact zone (total nine). Figure 52(b) shows the dimensions of the aluminum shear ties.

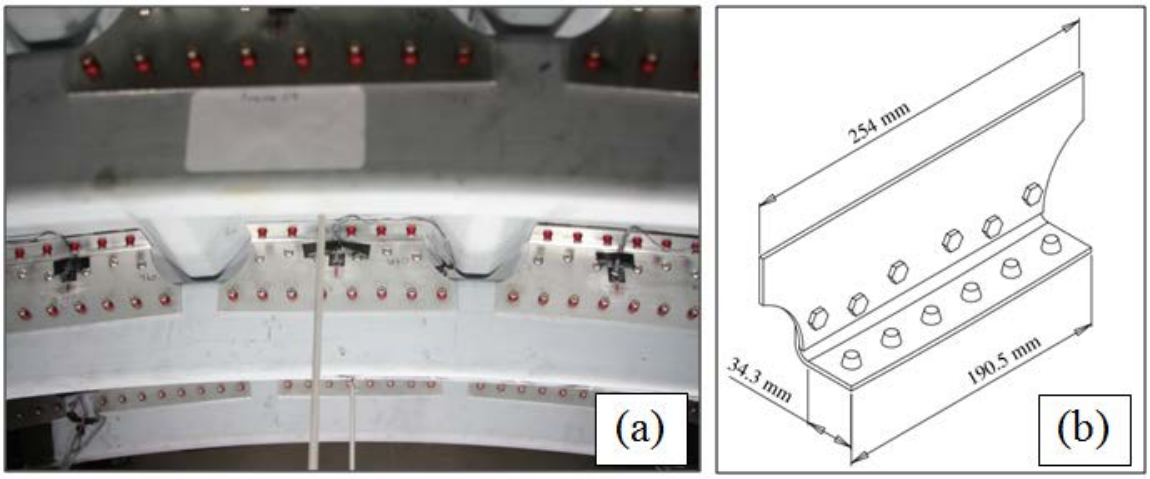

Figure 52. The aluminum 7075 shear ties (a) mounted to the Frame04 panel, and (b) overall dimensions

The Frame04-2 panel was then tested following the same test setup and loading as Frame03 and Frame04-1. Figure 53 shows the contact force versus skin indentation of the Frame04-2 specimen test plotted along with the combined plot for the Frame03 and Frame04-1 tests. As expected, the stiffer and stronger aluminum shear ties did not experience the brittle-like quick fracture failure exhibited by the carbon fiber shear ties. In addition, the lack of a laminated construction allowed the aluminum shear ties to carry much higher load before failure because the delamination failure mode was absent in the aluminum shear-tie curved region. Consequently, impact of the Frame04-2 specimen generated higher peak contact force of 125.4 kN before the initiation of failure. The aluminum shear ties, by not failing, did not allow for any energy release mechanism. Therefore, the reinforcing C-frames experienced high local stresses at the bolted connection between the aluminum shear ties and the C-frames.

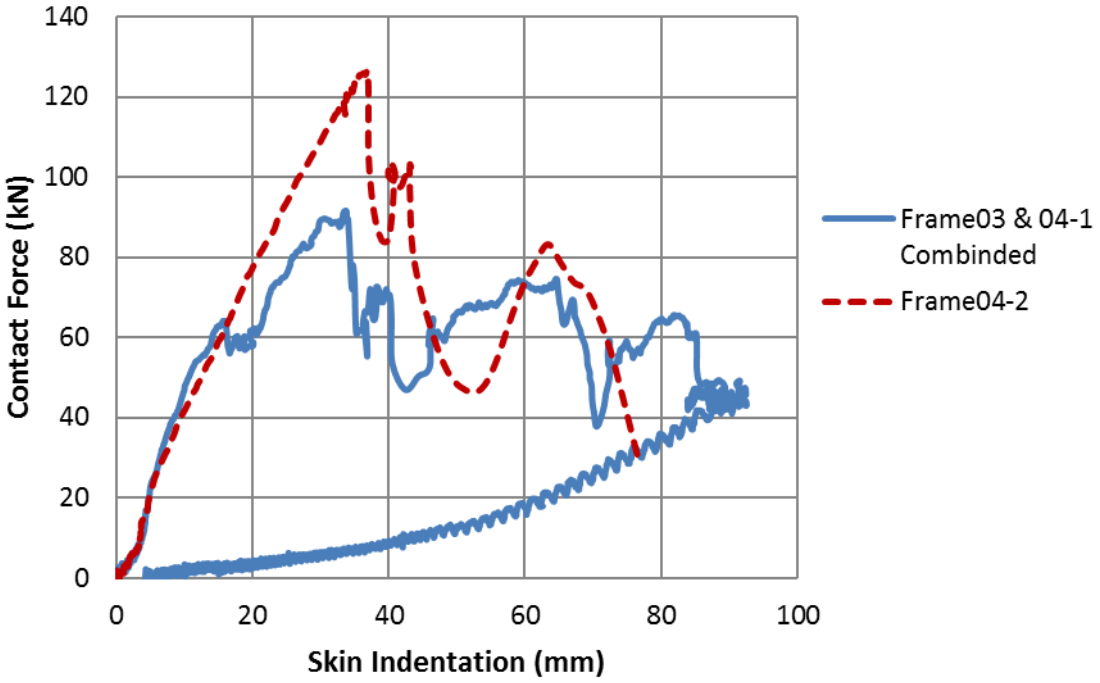

Figure 53. Contact force vs. skin-indentation plot of Frame04-2

In figure 53, three load drops were observed that corresponded to the sequential fracture of each C-frame. Localized shear fracture failures were observed in all three C-frames, as shown in figure 54 (high-speed video still taken during failure event). Minor exterior cracking of the skin developed from the panel's curved free edges where the stringers terminated with the panel edge. These cracks likely would not have developed in the absence of the free edge; furthermore, the Frame04-2 test significantly overdrove the actuator, with skin indentation of 40–50 mm producing major frame failures, thereby reducing the minor skin cracks formed. Although the frame shear-out failure mode was localized near the location of impact, and the specimen carried significantly higher peak loads, this configuration with stronger shear ties led to major C-frame failure as both the initial and final failure mode, without any intermediate failure modes that would perhaps be less detrimental to residual structural capability (i.e., crushed shear ties less detrimental than cracked frames).

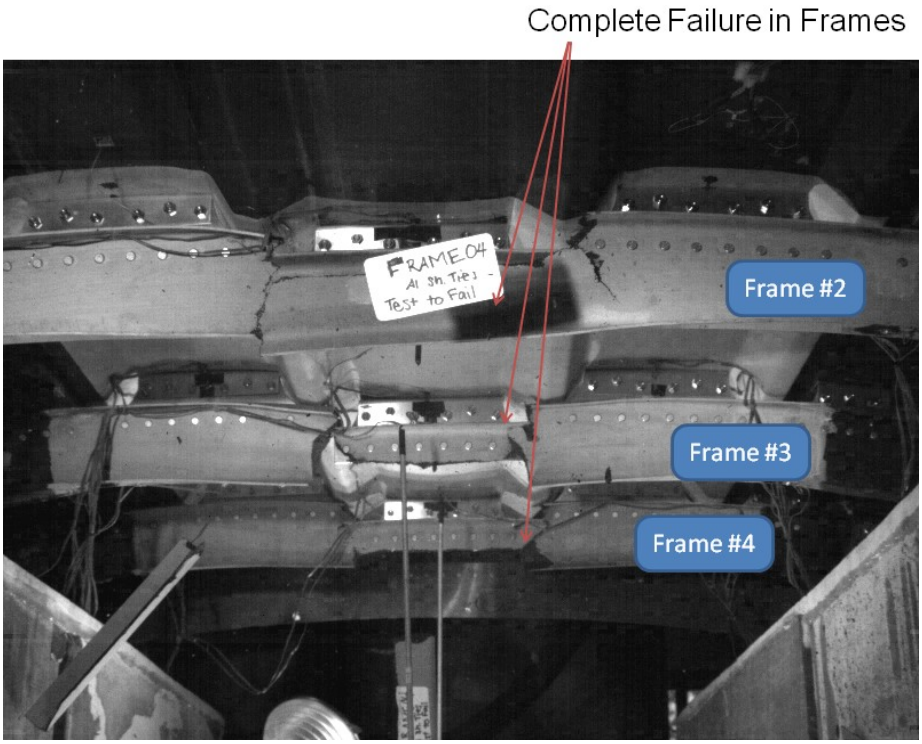

Figure 54. Frame04-2 local shear failure of the C-frames under the impactor

5. DISCUSSION AND CONCLUSIONS

5.1 STRINGERXX SPECIMENS DISCUSSION

Regardless of the test configuration, damage in the StringerXX specimens always initiated at the shear ties due to the downward compression and moment loading on the shear ties (see figure 55). Opening moment was induced by both skin rotations at the shear-tie supports and lateral movement of the panel, resulting in interlaminar tension stress at the shear-tie corners (i.e., radial-direction tension stress acting through the laminate thickness). The composite material's interlaminar tension strength is low, typically in the range of 40–50 MPa (mode I interlaminar fracture toughness of approximately 700 J/m^2). Therefore, shear-tie delamination was the first failure mode developed. As the compression load was increased, fiber breakage at the shear ties was also found because of crushing from the impact load.

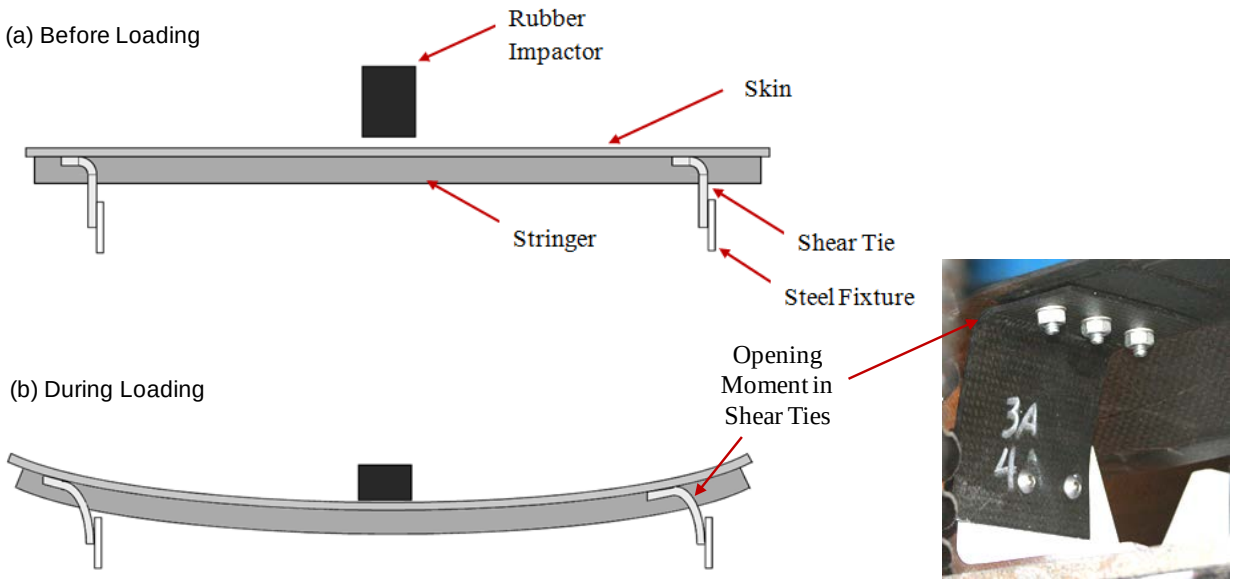

Figure 55. Side view of StringerXX panel: (a) before impact loading, and (b) during impact loading; compression and opening moment loading are exerted on the shear ties

The shear-tie failures were minor failure modes because of their progressive nature and, although having minimal effect on the structural integrity of the stringer-stiffened panel, would affect load transfer from the skin to the frames. Furthermore, the existence of damaged shear ties could serve as an indicator that a HEWABI event has occurred (reported or not) and that other internal damage could be present in the area. Increasing the visibility of damage in the shear ties (e.g., painting them white) could serve to aid in visual inspection for damage in the shear ties.

Conversely, major failure modes observed were strongly dependent upon the impactor type, impact location, and impact speed. These major failure modes included skin penetration, stringer delamination from the outer skin structure, skin cracking, and stringer fracturing. Skin-penetration damage occurred in impact tests involving a hard metal impactor because of the localized contact stresses around the periphery of the impactor. Stringer-to-skin delamination occurred in cases in which a soft rubber impactor was used. The rubber impactor reduced the local contact stresses at the impact site and suppressed penetration damage at the direct location of impact. As higher loads were built up, the interlaminar shear stresses between the stringer and the skin eventually led to the development of delamination damage.

Blunt-impact-induced damage to stringer-reinforced composite panels could be externally visible (skin penetration and cracking) or masked (skin-stringer delamination). Damage could also be localized or widespread. These damage characteristics were strongly dependent on impactor sharpness, impact location, and impact velocity. Figure 56 summarizes the effects of these three factors on damage visibility. First, the impactor stiffness and impact locations affect the panel deformation by changing the local contact stiffness between the impactor and the panel surface. Higher contact stiffness generated higher contact stresses, which created localized skin cracking with increased external visibility at the point of impact. Conversely, lower local stiffness reduced the contact stresses (allowing higher loads) and generated widespread internal damage along the load path, particularly at points of stiffness change and joints. This internal damage was obscured

from the external surface view. Secondly, the impact speed contributed to stress and damage localization by changing the deformation mode shape. Higher speed impacts resulted in higher-order deformation mode shapes confined around the impact zone, whereas quasi-static loading resulted in first-order mode shapes (see figure 41). It was found that, unlike previous studies on smaller composite plates, the dynamic response of large-sized fuselage panels did have an important effect on the specimen response, even for low-velocity (0.5 m/s) loading speed.

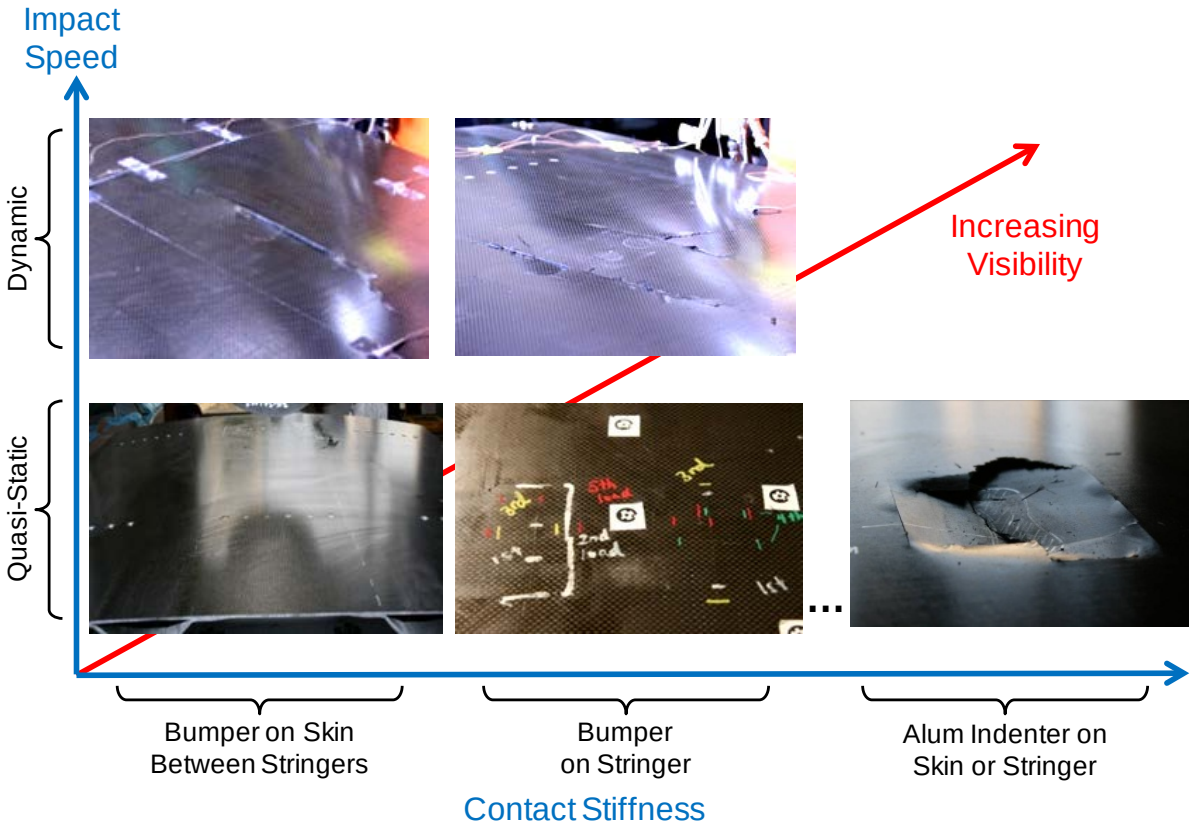

Figure 56. General trend of damage based on the StringerXX series experiments

5.2 FRAMEXX SPECIMENS DISCUSSION

Although the StringerXX specimen focused on damage modes in the stringer-skin panel and shear ties, it did not include frames. Therefore, larger-sized FrameXX specimens were fabricated and tested. When the FrameXX specimens were loaded on the skin between the stringers, the impact loading was transferred directly into the shear ties and the C-frames. In response, the shear ties in the impact zone delaminated at the curved radius region and subsequently fractured in compression and bending. With the directly loaded set of shear ties fractured, the load path was redirected to the shear ties located one bay away from the loading. For increasing applied impact forces, the C-frames deformed in bending and twisted because of load eccentricity (loading applied away from their shear centers), and the C-frames eventually contacted the stringers. In the case of the quasi-statically loaded specimens, a contact lock was formed between the stringers and C-frames. Therefore, high-contact stresses led to failures, such as local crack formation and penetration (stringers into frame, and frame into stringers) in the affected C-frames and the stringers.

A different damage mechanism was found in the dynamic experiments (Frame03), in which the C-frames experienced large twisting deformation after the shear ties fractured. Rather than being restrained by contact locking with the stringers, the C-frames twisted continuously and scraped against the stringer's surface (dynamically sliding) until failure occurred. This led to fracture of the C-frames in combined torsion, shear, and bending mode at locations away from the load-application location, near the fixture boundaries (i.e., along load path to surrounding structure).

Whereas stringer delamination and stringer cracking were the major damage modes for the StringerXX series of experiments, the FrameXX specimen failures were more complex because of their larger size and the addition of C-frames. The wider impact zone allowed for direct load transfer from the bumper to the shear ties and C-frames. Skin-stringer delamination was not a major failure for these specimens because of the main load path going into the frames. Fiber-cracking failure was found in the internal structural elements, including the shear ties, C-frames, and stringers.

5.3 RELATION TO GROUND THREATS

The experiments reported on were conducted in a displacement-control mode, either under quasi-static or dynamic conditions. This is a departure from the scenario of GSE rolling in with initial velocity and decelerating as it contacts and impinges into the aircraft. Alternatively, the operation of vehicular GSE by persons manually controlling an accelerator and brake could actually be similar to the displacement-control loading: The incoming GSE must be stopped fully and then put into reverse gear before withdrawing away from the aircraft.

Force versus displacement data measured during the blunt impact tests reported herein can be related to ground threats via energy balance. Specifically, the energy dissipated by the deforming and fracturing composite structure is equal to the area under the force versus displacement curve, leading up to that level of displacement. This is shown in figure 57, which plots the force versus displacement data of specimen Frame03 (dynamically loaded at 0.5 m/s across three frames). The initial major failure mode for which the first set of directly loaded shear ties fractured (indicated as D1 in figure 57) is associated with 600 J of energy at a skin indentation level of 20 mm. Further driving in of the skin produces additional levels of internal damage severity, accompanied by increasing energy levels. For fracture of the frames, an additional 3600 J energy is needed at a skin indentation level of 80 mm.

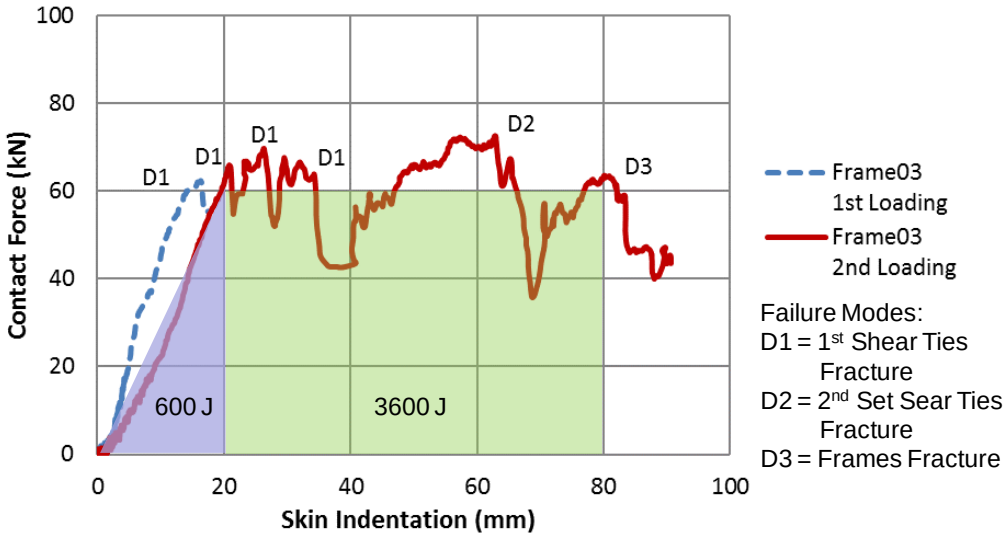

Figure 57. Frame03 force versus displacement data with energy associated with 1st shear ties fracturing (600 J) and with frames fracturing (600 + 3600 J)

Considering GSE rolling into an aircraft as a heavy mass coming in with initial velocity, the kinetic energy of this large-mass GSE projectile can be calculated and compared with the energy levels associated with the development of various levels of damage. This accounts for local effects, and the global response of the entire aircraft interacting with the heavy GSE can be considered as a multi-degree-of-freedom (DOF) dynamic system (see figure 58). In this type of model [4], the interaction between aircraft and GSE has been modeled as a nonlinear spring to account for the crushing deformations of the GSE as it indents into the aircraft.

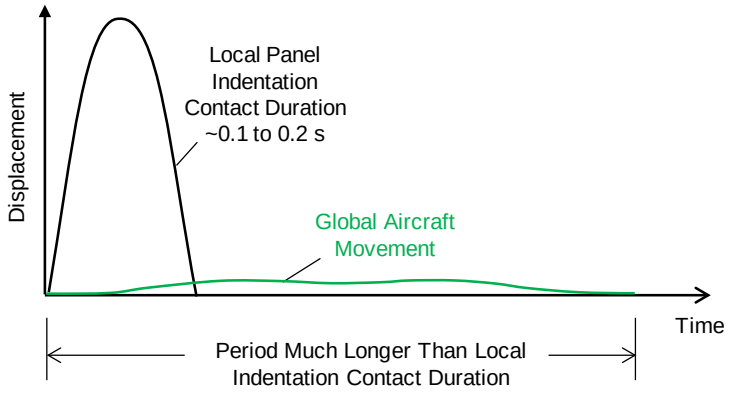

Figure 58. Simple model description of GSE impacting full aircraft [4]

By assuming typical masses of GSE and aircraft (e.g., 10,000 kg and 200,000 kg, respectively), the dynamic interactions between the local panel indentation displacement and global motion of the aircraft can be assessed. Such analyses have shown, for realistic levels of stiffness assumed in the models, that the global aircraft response occurs at a significantly longer time scale than the interaction of the GSE impinging into the aircraft, thereby eliminating or greatly reducing the dependency of the local damage response (at site of GSE impact) on the global (rigid-body like)

motion of the aircraft. This comparison of time scales and deformation response is shown conceptually in figure 59 (see reference [4] for further model details and sample calculations). Therefore, a first-order energy balance treatment of the local indentation deformation could be decoupled from the global motion of the aircraft if the period of oscillation for the global motion is more than three times longer than for the local indentation or if the global motion is much lower in magnitude than the local indentation deformation.

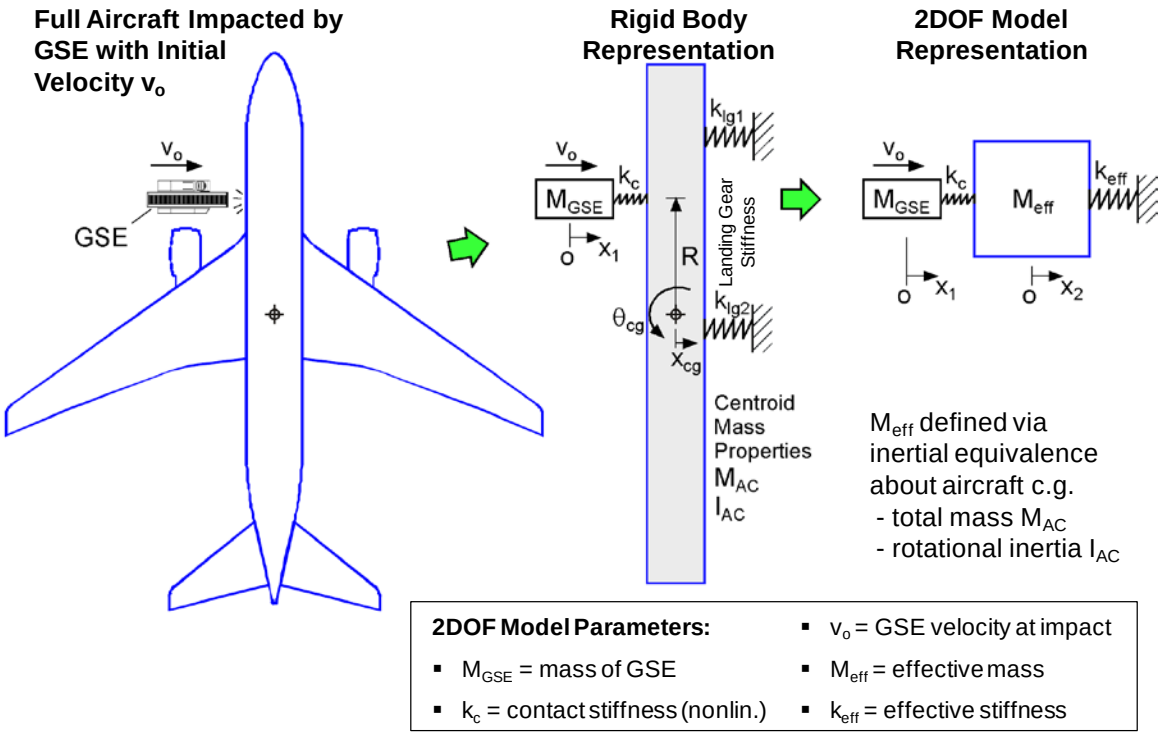

Figure 59. Conceptual local panel indentation displacement compared to global aircraft motion time history, based on detailed calculations using representative values of mass and stiffness in 2DOF nonlinear spring model [4]

5.4 BLUNT IMPACT DAMAGE LENGTH SCALE

Blunt impacts can be defined as impact sources that can affect large areas or multiple structural elements, but potentially leaving little or no externally visually detectable signs of damage. Blunt impacts come from a variety of sources and can involve a wide range of energy levels. Whereas the side- and lower-facing surfaces of the aircraft are subject to contact with GSE, all exposed upper and vertical surfaces are subject to other blunt sources, namely ground hail impact (terminal velocity + wind gust), and forward-facing surfaces are subject to in-flight high-velocity hail impacts. Upward-facing surfaces are also subject to tool-drop impact. These various blunt impact sources have been studied at UC-San Diego and are described in more detail below:

1. Impact/contact by GSE includes ground vehicles, cargo loaders, and any other equipment [4–6] coming in close proximity to a commercial aircraft. GSE is a source of great damage potential because of the high mass of the GSE (typically 3,000–15,000 kg) and the subsequently high energies involved. Figure 60 shows the kinetic energy levels of GSE to

be up to the 10^3 J range (e.g., 10,000 kg cargo loader moving at 2 mph, or 0.894 m/s, has 4,000 J of kinetic energy). The length scale of contact for GSE impact can range from ~20 cm for a belt loader's single D-shaped bumper to more than 2 m for a long cargo loader bumper (both shown in figure 60). It should be noted that GSE historically accounts for a major percentage of damage occurring to commercial transport aircraft [1] and is expected to continue to be a major source regardless of whether the aircraft is made from aluminum alloy or carbon/epoxy composite.

2. Hail ice impacts have been studied at UC-San Diego as another source of blunt impact [7–10]. These involve high velocities and, therefore, high energy levels, exceeding 1,000 J (see figure 60), mainly by virtue of typical aircraft in-flight speeds (more than 200 m/s). Even higher velocities (energy) are possible for rotating components like helicopter rotor and engine fan blades. Ground hail occurs at lower energy levels, with relatively high velocity, ranging from 20–30 m/s, which excites a localized dynamic response in the impacted structure. The ice projectile is complex in that it exhibits an initial elastic-type response and then severely crushes during the course of impact [7–9, 11]. This crushability results in a larger zone of contact, as shown in figure 60 [9], which significantly reduces the propensity to impart visual damage. Meanwhile, ice impact can produce significant internal damage, such as large-area delamination [7, 8, 10], skin-stringer separation [9, 12], and internal sandwich core crushing [13, 14] with no external visibility, unless penetration is achieved.

3. Low-velocity impacts by metal tips of a large radius (greater than 76 mm) have also been investigated [15–18] as a representation of impacts by generic sources, such as dropped tools or equipment, or contact with GSE features that are not covered by rubber bumpers (e.g., railings and rounded corners). The results of impacts by large radius tips are contrasted with a 12.7 mm radius (1.0 in. diameter) tip that is most commonly used for creating barely visible impact damage of a specified dent depth (e.g., 0.3 mm).
   The 12.7 mm radius tip damage source, although commonly employed as part of an airframe component's damage-tolerance program, may not be representative of actual blunt sources (often of unknown geometry) of damage, which can involve higher energy levels. Larger radius tips allow higher contact forces to be applied before a dent or other externally visible evidence of damage is left on the impacted surface.

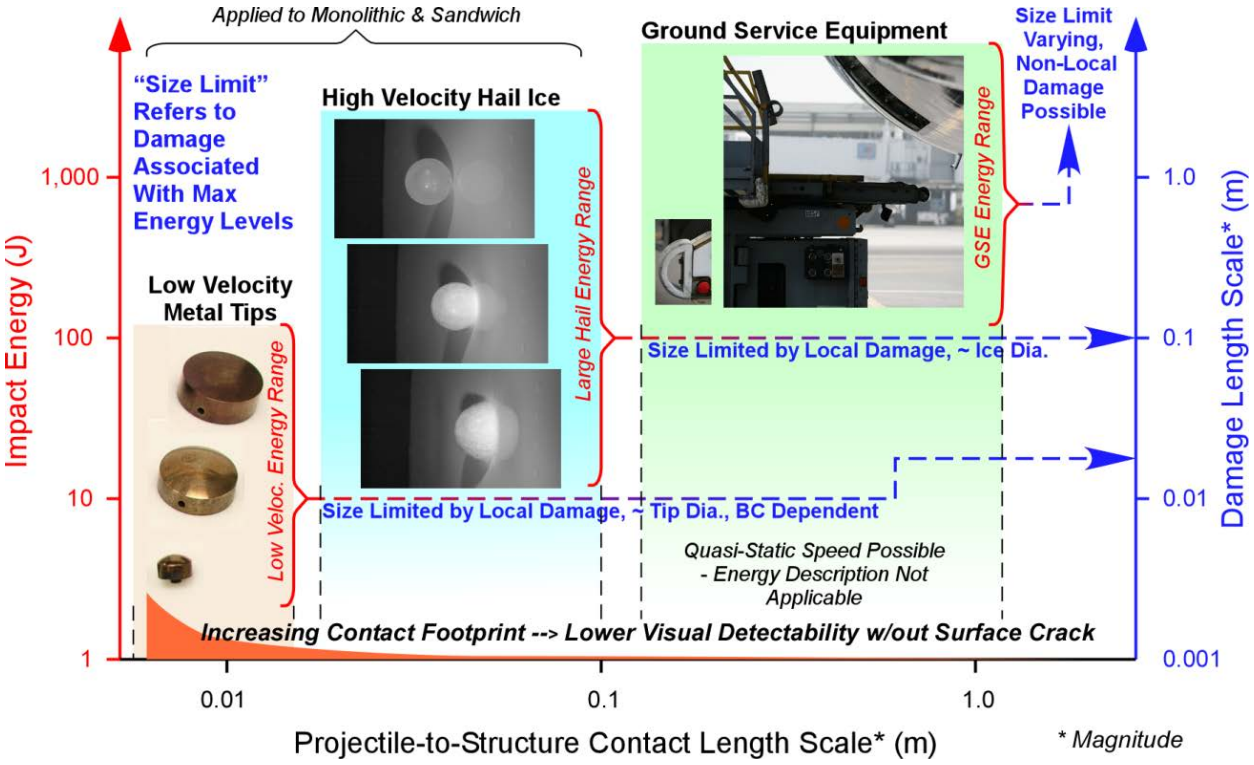

Figure 60. Blunt impact energy-damage spectrum

Among the three impact sources being studied at UC-San Diego (see figure 60), both the low-velocity metal tips and high-velocity ice impact can usually be associated with a damage size limit (see right-hand axis in figure 60). This damage limit reflects the ability for these impact sources to induce localized failure at the point of impact/contact. Therefore, maximum-level cases of velocity and energy will typically produce penetration damage because of this localized response. Penetration damage has a size limit roughly equivalent in dimension to the impacting projectile (see figure 60). For this reason, the worst-case scenario might not always produce the most critical mode(s) of damage.

For the GSE impact, a non-local response has been observed to be possible. Specifically, internal damage can occur at locations away from the point of impact/contact (e.g., at joints or stress concentrations along the internal load path to the surrounding structure). Therefore, the damage size limit is not clearly known and, depending on the severity (energy level) of the impact event, can possibly be larger than the length scale of the contact between the projectile and structure. Furthermore, the GSE contact speed can be quite varied, even a very slow (quasi-static) level, as indicated in figure 60, so the energy-based description might not fully describe GSE-aircraft interactions.

5.5 CONCLUSIONS

Composite test specimens having features found in modern transport aircraft fuselage construction were designed and fabricated. Blunt quasi-static indentation and blunt-impact tests have shown that significant internal damage can develop from high-energy wide-area blunt impact (HEWABI) events, potentially with little to no external visually detectable indicators that a damage-producing event has occurred. HEWABI involves large-area contact, often with a soft interface (bumper/spacer made of rubber/elastomeric materials), which serves to greatly lower contact stresses local to the immediate location of impact, thereby reducing the chance of producing surface-visible skin cracks or even surface scratches. The contact area during impact is a key parameter driving overall size (extent) of damage and determining whether damage forms local to impact site or globally along the load paths transmitting contact forces into surrounding internal structure. Therefore, a damage search following a HEWABI event should include inspection of the internal structure along these load paths (1 m length scale away) and locations around the aircraft at which GSE were closely docked (10 m length scale), as HEWABI would induce significant global motion of the aircraft. High-strength composite external skins are able to deform significantly without cracking and permanent deformation to the skin. This is in contrast to ductile metal (e.g., aluminum alloy) skins, which yield and, therefore, have a higher chance of forming visually detectable residual dents. The use of such high-strength resilient composite skins presents a challenge to the visual-detection-based paradigm of damage detection by which aluminum-based aircraft have been managed.

5.6 RECOMMENDATIONS

Future work recommendations include additional tests to investigate:

- Shear-tie configurations having more continuous geometry, in comparison with the discontinuous shear ties reported here.
- Frame-to-floor joint connection stiffness—essentially more realistic boundary conditions on the frames accounting for compliance of interaction with the stiff floor beam assembly.
- Glancing angle effects, particularly in the lower fuselage zone near the cargo floor plane. This necessitates a larger-sized portion of structure to be tested (e.g., full quarter barrel).

In addition to testing, general modeling capability development for predicting observed failure modes is needed to establish clear methodologies for how to predict blunt-impact damage and how to establish thresholds of damage initiation. More extensive modeling can also be used to increase understanding of the global motion effects relative to GSE strike location and velocity.

6. REFERENCES

1. International Air Transportation Association (2005). "Ground Damage Prevention Programme Targets 10% Cost Reduction," Industry Times, Edition 7, September, Article 4.

2. Kim, H., Kedward, K. T. (2000). Modeling Hail Ice Impacts and Predicting Impact Damage Initiation in Composite Structures. *AIAA Journal, 38*(7), 1278–1288.

3. Kim, H., Kedward, K.T., Welch, D.A. (2003). Experimental Investigation of High Velocity Ice Impacts on Woven Carbon/Epoxy Composite Panels. *Composites Part A: Applied Science and Manufacturing 34*(1) 25–41.

4. Kim, H., DeFrancisci, G. K., Chen, Z. M. (2012). *Estimation of ground service equipment contact damage in composite aircraft panels*. Proceedings from the 53rd AIAA/ASME/ASCE/AHS/ASC Structures, Structural Dynamics, and Materials Conference, Honolulu, HI.

5. DeFrancisci, G.K. (2013). "*High Energy Wide Area Blunt Impact on Composite Aircraft Structures*" (Ph.D. Dissertation). University of California, San Diego, CA.

6. Chen, Z.M. (2015). "*Experimental and Numerical Investigation of Wide Area Blunt Impact Damage to Composite Aircraft Structures*" (Ph.D. Dissertation). University of California, San Diego, CA.

7. Rhymer, J., Kim, H., Roach, D. (2012) The Damage Resistance of Quasi-Isotropic Carbon/Epoxy Composite Tape Laminates Impacted by High Velocity Ice. *Composites Part A: Applied Science and Manufacturing, 43*(7) 1134–1144.

8. Rhymer, J.D., "*Force Criterion Prediction of Damage for Carbon/Epoxy Composite Panels Impacted by High Velocity Ice*" (Ph.D. Dissertation). University of California, San Diego, CA.

9. Le, J.L. (2013). "*Hail Ice Damage of Stringer-Stiffened Curved Composite Panels*" (M.S. Thesis). University of California, San Diego, CA.

10. Funai, S. (2012). "*Hail Ice Impact on Composite Structures at Glancing Angles*" (M.S. Thesis). University of California, San Diego, CA.

11. Tippmann, J.D., Kim, H., Rhymer, J.D. (2013). Experimentally Validated Strain Rate Dependent Material Model for Spherical Ice Impact Simulation. *International Journal of Impact Engineering, 57*, 43–54.

12. Park, H., Kim, H. (2010). Damage Resistance of Single Lap Adhesive Composite Joints by Transverse Ice Impact. *International Journal of Impact Engineering, 37*(2), 177–184.

13. Kim, H., Anagnostopoulos, K., Chan, M., Luong, S. (2015). *Internal impact damage to lightweight composite sandwich panels*. Proceedings from the 30th American Society of Composites Annual Technical Conference, E. Lansing, MI.

14. Luong, S.D. (2014). "*Hail Ice Impact of Lightweight Composite Sandwich Panels* (M.S. Thesis). University of California, San Diego, CA.

15. Whisler, D., Kim, H. (2012). Effect of Impactor Radius on Low Velocity Impact Damage of Glass/Epoxy Composites. *Journal of Composite Materials, 46*(25). 3137–3149.

16. Whisler, D., Kim, H. (2016). *Low velocity impact damage and response of stringer stiffened composite panel*. Proceedings from the 31st American Society for Composites Annual Technical Conference, Williamsburg, VA.

17. Delaney, M.P. (2013). "*Low Velocity Impacts of Variable Tip Radius on Carbon/ Epoxy Plates*" (M.S. Thesis). University of California, San Diego, CA.

18. Chan, M.K. (2014). "*Low Velocity Blunt Impact on Lightweight Composite Sandwich Panels*" (M.S. Thesis). University of California, San Diego, CA.